Version of Record: https://www.sciencedirect.com/science/article/pii/S0022509621002593
Manuscript_e5a8aff38b511a09ee29846e78792324

Energy based fracture initiation criterion for strain-crystallizing rubber-like materials with pre-existing cracks

Prajwal Kammardi Arunachala, Reza Rastak, Christian Linder*

Department of Civil and Environmental Engineering, Stanford University, Stanford, California, 94305, USA

Abstract

Fracture prediction is indispensable for polymers, like rubbers, which have a broad range of applications mainly due to their high extensibility. The phenomenon known as strain-induced crystallization further contributes to the fracture toughness of certain rubbers. In this study, a criterion based on internal bond energy, incorporating the effects of crystallization, is proposed to predict fracture initiation in rubber-like materials with pre-existing cracks. First, a multi-scale mechanical model is developed for characterizing the behavior of rubber when subjected to both uniaxial and biaxial deformation states. At the microscale, both the amorphous and crystalline chain segments are modeled as elastic in order to consider the energy contribution by the molecular bond distortions. This internal energy is considered along with the entropic and crystalline free energy for each chain. In the chain model, the effects of loading condition and the relative orientation of a chain on its crystallinity are taken into account. At the macroscopic scale, an existing crystallinity distribution function is adapted and a mixed finite element formulation with an augmented Lagrangian multiplier is utilized to impose the incompressibility constraint. A non-affine maximal advance path constraint based homogenization model is utilized for bridging the two scales. Its potential to account for anisotropy in the stretched network compels the model to be preferable due to its physical significance, for the purpose of fracture modeling. The rigidity of the crystallites is accounted for by proposing a crystallite distortion energy in addition to the critical bond dissociation energy, for fracture initiation to occur. The model is validated by comparison with existing experimental results for both crystallizing and non-crystallizing rubbers. In addition to its potential to predict the material behavior when subjected to uniaxial and biaxial loading, the capability of the model to quantitatively estimate the effect of crystallization on fracture initiation is also verified.

Keywords: Fracture initiation, Strain-induced crystallization, Maximal Advance Path Constraint, Multi-scale model, Rubber, Biaxial loading

1. Introduction

The high stretchability of many polymers prior to their fracture make them a perfect choice in applications such as self-actuators, epidermal electronics and implantable sensors. This has led to a surge in experimental and computational works focusing on the study of such polymers (Li et al., 2020; Wang et al., 2017; Wang and Chester, 2018). Additionally, desirable properties like high toughness, low cost and lower weight result in rubber-based materials having a wide range of industrial applications like tires, seals, hoses and airbags (Loew et al., 2019; Hashemi et al., 2020; Mittal et al., 2011). Thus, predicting the fracture initiation point is paramount to design against fracture or fatigue failures.

In general, the underlying polymer networks of the rubber-like materials, whose crosslinks and chain entanglements provide elasticity, are mainly responsible for their stretchability. Interestingly, natural rubber (NR) and certain synthetic rubbers like polyisoprene rubber (IR) exhibit much higher strengths than other similar polymers like styrene butadiene rubber (SBR) (Clamroth and Kempermann, 1986). In many attempts that have been made to unravel this

*Corresponding author
Email address: linder@stanford.edu (Christian Linder)

mystery, the phenomenon called strain-induced crystallization (SIC) has been attributed to be the inducer of the higher fracture resistance (Lake and Thomas, 1967; Mars and Fatemi, 2004; Toki, 2014; Tee et al., 2018).

SIC involves the phase transformation from an amorphous solid to a partially crystalline solid upon the application of a large amount of stretch in certain polymers having conducive chemical composition for the phenomenon to take place. Ever since Katz (1925) discovered the phenomenon of SIC using the state-of-the-art X-ray diffraction method, there have been many experiments studying the effects of crystallization on the material properties (Gehman and Field, 1939; Candau et al., 2014; Toki et al., 2003; Tosaka et al., 2004; Brüning et al., 2012; Chen et al., 2019). The toughening effect of the phenomenon on the fracture properties of crystallizing rubbers has also been experimentally studied (Rublon et al., 2014; Trabelsi et al., 2002; Zhang et al., 2009; Gherib et al., 2010; Brüning et al., 2013a,b).

One of the earliest theoretical formulations of SIC was done by Flory (1947) wherein Gaussian statistics was used, and the equilibrium condition of the process was considered. Since then, many studies have improved on this by considering non-Gaussian statistics (Smith Jr, 1976), non-equilibrium kinematics (Gent, 1954) and multi-scale bridging (Kroon, 2010; Mistry and Govindjee, 2014; Guilie et al., 2015; Rastak and Linder, 2018; Khiêm and Itskov, 2018; Gros et al., 2019). However, a majority of these studies restrict their attention to describe the SIC phenomenon for the uniaxial tensile loading case. A primary reason for this is the lack of experimental studies focusing on material behavior when subjected to more elaborate deformations. Recently, Chen et al. (2019) experimentally observed a frustration in SIC when a specimen made of NR was subjected to biaxial tension. Thus, there is a need for a more comprehensive model encompassing such experimental findings for different states of deformation.

Though there are copious models for describing the phenomenon of SIC, there is a scarcity of models predicting its effect on the fracture properties. The main reason for this is that all of these models consider the classical representation of the polymer chains, wherein they are composed of freely rotating rigid segments. Thus, these studies concentrate mainly on the free energy due to entropy in the chain and that due to crystallization while neglecting the change in internal energy due to stretching of the constitutive atomic bonds. However, Lake and Thomas (1967) argued that the polymer chain rupture occurs due to the breaking of the molecular bonds and hence is dominated by the internal energy.

Even though good multi-scale theories are developed at both the microscopic and macroscopic levels, their effectiveness highly depends on the link that bridges the scales. The early network theories like the 3-chain model (James and Guth, 1943; Wang and Guth, 1952) assumed affine deformation, which considered the deformation mapping to be the same for both scales. However, this was observed to over-constrain the system, by hindering the process of redistribution of stress by chain reorientation for attaining a lower energy state. This has been overcome by the concept of non-affine deformation which allows for the chain reorientation while satisfying the kinematic compatibility conditions at the same time. The 8-chain model by Arruda and Boyce (1993) considers an affine deformation of representative chains along the diagonals of a unit cubic cell, in order to derive an effective non-affine network response. The non-affine microsphere model by Miehe et al. (2004) adopts a continuous space of chain orientations in a unit sphere and proposes a constraint for polymer network deformation. However, both the models assume isotropic behavior resulting in an equal stretch of deformed polymer chains in all directions. In contrast, another network homogenization model called the Maximal Advance Path Constraint (MAPC) developed by Tkachuk and Linder (2012) has been proven to account for anisotropy during the study of SIC in Rastak and Linder (2018). As chains with larger stretches can rupture and trigger a failure of the network, anisotropic models like MAPC are better suited for fracture applications due to their capability of singling out such chains. However, so far, there is a lack of studies utilizing this theory for modeling fracture in polymers.

The prediction of fracture initiation and complete rupture in rubber-like materials has been mostly phenomenological, using just their macroscale properties. Similar to the Griffith (1921) criterion, Rivlin and Thomas (1953) utilized a characteristic tearing energy based criterion to predict incipient and catastrophic tearing of natural rubber test specimens. This theory was extended from single edge notches to double edge ones using the J-integral by Hocine et al. (2002). In other studies, Kawabata (1973) proposed a criterion for fracture during biaxial stress states determined by a critical stretch, and this was extended to different biaxiality loading ratios by Hamdi et al. (2006). Recently, Kumar et al. (2018) and Kumar and Lopez-Pamies (2020) have developed a phase-transition model for elastomers considering fracture nucleation in regions of large hydrostatic stress concentrations and crack propagation consistent with Griffith's theory. Although Griffith's theory works well for specimen with macroscopic flaws, Chen et al. (2017) experimentally demonstrated that its underpinning assumption of flaw-sensitive behavior does not hold good at very small length scales, which range from nanometers to centimeters depending on the material. In addition, fracture

models accounting for the micro-mechanical aspects of the polymer material are advantageous for augmenting the effects of complex microscale phenomenon like SIC.

In a landmark fracture study using the microscopic aspects of polymer networks, Lake and Thomas (1967) followed a critical internal energy approach for predicting fracture initiation in polymer networks. Mao et al. (2017) built upon this theory by bridging the micro and macro scales using the eight-chain network model and postulated a fracture initiation criterion for elastomers with flaws, based on molecular bond disruption energy. Unlike other phase-field fracture models for rubbers like Miehe et al. (2004) and Loew et al. (2019) which utilize the macroscopic critical energy release rate theory, Talamini et al. (2018) developed a fracture model employing the microscopic critical internal energy formulation. However, there have been no studies explicitly predicting the crack initiation or propagation through crystallizing rubbers.

Building models to predict crack initiation in rubber-like polymers is paramount due to their wide scope of applications. In particular, crystallizable rubbers have high toughness and hence it is vital to study the effect of SIC on their fracture resistance. Motivated by this, we have postulated an energy-based criterion incorporating the effects of crystallization to predict fracture initiation in rubber-like polymers with pre-existing cracks. The mechanics-based multi-scale model for characterizing the polymer behavior, which is coupled with the criterion, is applicable to even biaxial loading cases. Modeling the crystallized chain segments as elastic by considering the internal energy contribution due to molecular distortions, taking into account the effects of loading condition and the relative orientations of chains on their crystallinity, utilization of an anisotropic network model for fracture prediction, and accounting for the effects of crystallization for predicting fracture initiation, are some of the primary features of this model. Although viscous effects have been observed in rubber-like materials, many studies (Hamed and Park, 1999, Gherib et al., 2010, Hamed, 2005, Zhou et al., 2014, Mars and Fatemi, 2004) highlight the dominant effect of SIC on the fracture properties of crystallizing rubbers. Hence, this study mainly focuses on quantifying the effect of crystallization on their fracture initiation while neglecting viscous effects.

The outline of the paper is as follows. In Section 2, the multi-scale micro-macro approach is presented for modeling the behavior of rubbers. The chains and their segments are modeled at the microscopic level in Section 2.1 and Section 2.2. While the deformation in both the micro- and macroscales are linked together using the MAPC network homogenization model in Section 2.3, the crystallinity variables are linked in Section 2.4. In Section 3, the fracture initiation criterion for non-crystallizing rubbers is first postulated in Section 3.1 and then extended to include crystallizing rubbers in Section 3.2. The numerical implementation of the algorithm using a mixed finite element formulation is explained in Section 4. Experimental results are used to validate the model in Section 5. Finally, after stating the major conclusions from the study in Section 6, some advanced concepts, derivations and additional results are presented in the appendices.

2. Multi-scale approach for polymer behavior characterization

It is a well-known fact that rubbers have underlying polymer chain networks which are one of the main reasons for their unique characteristics. Thus, modeling a chain at the microscopic scale is vital to comprehend the rationale behind their behavior. Macroscopic-scale modeling is required for understanding their response to external actions. These models are connected using network models, which mostly constrain microscopic motions so that they are kinematically compatible with the macroscopic deformations.

In this study, behaviors of rubber-like polymers at microscopic and macroscopic scales are modeled, which are then combined with the help of a non-affine deformation model. The microscopic scale involves polymer chains made up of a number of segments. A continuum formulation can be utilized for modeling the macroscopic behavior of the material. The bridging of these two scales is accomplished by using a non-affine model called the Maximal Advance Path Constraint (MAPC).

Similar to our previous study in Rastak and Linder (2018), chain stretch λ, chain force f, degree of crystallization ω and its rate $\dot{\omega}$ are considered as the main microscopic variables. In addition to this, chain segments are modeled to be elastic ensuing in a segment bond stretch λ_b. The continuum macroscopic model comprises of the isochoric deformation gradient $\bar{\boldsymbol{F}}$, its conjugate first-Piola Kirchhoff stress tensor $\bar{\boldsymbol{P}}$, the macroscopic continuous crystallinity variables $\boldsymbol{\Omega}$ and their conjugate rate $\dot{\boldsymbol{\Omega}}$ as the primary variables.

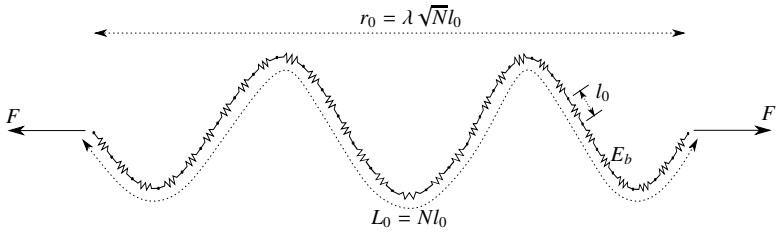

Figure 1: Chain model for fully amorphous chain with elastic segments

2.1. Microscopic description for non-crystallizing rubber

The high stretchability resulting from high elasticity is a fundamental property of rubbers. Attributing this mechanical behavior of rubbers to the entropy of chain molecules between crosslinks, classical theories model the chain with a series of freely jointed segments having equal lengths. Considering the chain segments as rigid is one of the simplifying assumptions that is commonly made. Polymer chains have been found to exhibit a statistical behavior as they always tend to exist in the most probable configuration. So, in this study, the non-Gaussian Langevin chain statistics is utilized for modeling polymer chains.

For representation, the number of segments in a chain and their individual lengths are denoted by N and l, respectively. Using the Gaussian theory, the initial end-to-end distance of a chain is given by its root-mean-square value $r_0 = \sqrt{N}l$. If the current end-to-end distance is denoted by r, then the stretch in the chain can be defined as $\lambda = r/r_0$.

The Langevin parameters estimating the stretch in the chain are given by

$$\Lambda = \mathcal{L}(\beta) = \frac{r}{L} = \frac{\lambda}{\sqrt{N}} \quad \text{(assuming rigid segments).} \tag{1}$$

In the above equation, Λ and β are the Langevin parameters, $\mathcal{L}(x) = \coth x - x^{-1}$ is the Langevin function, and $L = Nl$ is the total contour length of the chain. The Langevin parameter Λ physically represents the chain stretch normalized by the maximum possible end-to-end chain length. According to the non-Gaussian theory (James and Guth, 1943; Kuhn and Grün, 1942), the tensile force in the chain needed to overcome the thermal oscillations is given by

$$F = \frac{k_B T}{l}\beta\,. \tag{2}$$

The free energy of the chain due to entropy is obtained by integrating this force over the effective length of the chain and can be obtained as

$$\psi_a(\lambda) = \int_0^r F\left(r^\star\right)\mathrm{d}r^\star = k_B T N\left(\beta\Lambda + \ln\frac{\beta}{\sinh\beta}\right). \tag{3}$$

The force in the chain due to its stretch is given by

$$f = \frac{\partial\psi}{\partial\lambda} = l\sqrt{N}F = k_B T\sqrt{N}\beta\,. \tag{4}$$

This force is studied as a function of the stretch λ applied to the chain in Fig. 2a. It is observed that as the normalized stretch $\lambda/\sqrt{N} \to 1$, the normalized force $f/(k_B T\sqrt{N}) \to \infty$. This can be clearly explained on the basis of (1) wherein it is found that Λ tends to 1, thus forcing the other Langevin parameter β to tend to ∞. In addition to the inability of the classical theory to model material behavior at higher stretches, neglecting the bond distortion energy which dominates during fracture (Lake and Thomas, 1967) poses a challenge for studying the fracture properties of rubber.

The constraint was found to be a result of the assumption that chain segments are rigid. This neglects the stretch in the chain once its end-to-end distance starts approaching its contour length. This limitation was overcome by Mao et al. (2017), where they assume that the chain segments are elastic and introduce a stretch due to the extensibility of the molecular bonds, as illustrated in Fig. 1.

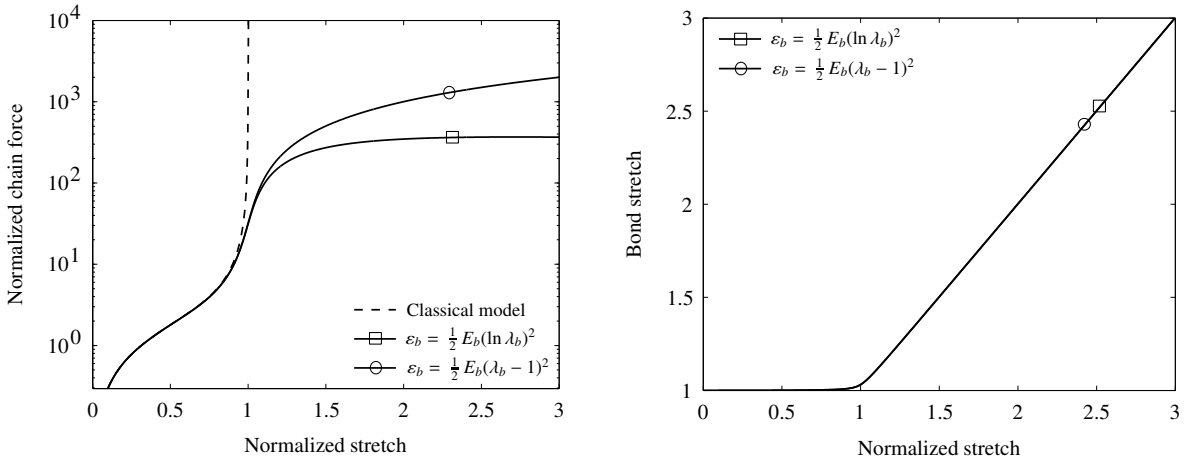

(a) Force-stretch response

(b) Bond stretch evolution

Figure 2: Constitutive chain response for the classical rigid chain segment model and the current elastic chain segment model with different internal energy expressions

This bond stretch, denoted by λ_b, can be defined as $\lambda_b = l/l_0$, the ratio of the current segment length to the initial one. So, (1) is modified as

$$\Lambda = \frac{r}{L} = \frac{\lambda r_0}{Nl} = \frac{\lambda \sqrt{N} l_0}{N \lambda_b l_0} = \frac{\lambda}{\lambda_b \sqrt{N}} \quad \text{(assuming elastic segments).} \tag{5}$$

In addition, the bond stretch also contributes an internal energy to the free energy of the chain. Therefore, the total free energy of a chain can be computed as

$$\psi(\lambda, \lambda_b) = \psi_b(\lambda_b) + \psi_a(\lambda, \lambda_b) = N\varepsilon_b(\lambda_b) + k_B T N \left(\beta\Lambda + \ln \frac{\beta}{\sinh \beta} \right). \tag{6}$$

The expression for the term $\psi_a(\lambda, \lambda_b)$ looks identical to (3) even with the introduction of the bond stretch λ_b, as shown by the derivation in Appendix A. The term $\varepsilon_b(\lambda_b)$ denotes the change in internal energy due to stretching in each chain segment. As explained in Mao et al. (2017), this bond stretch λ_b is the minimizer of the free energy for a given stretch λ and can be calculated by

$$\frac{\partial \psi(\lambda, \lambda_b)}{\partial \lambda_b} = 0 \implies \frac{\mathrm{d}\varepsilon_b}{\mathrm{d}\lambda_b} \lambda_b^2 = k_B T \frac{\lambda}{\sqrt{N}} \beta. \tag{7}$$

The canonical expressions of the internal energy due to bond stretch chosen for the study are $\varepsilon_b(\lambda_b) = \frac{1}{2} E_b (\ln \lambda_b)^2$ (Mao et al., 2017) and $\varepsilon_b(\lambda_b) = \frac{1}{2} E_b (\lambda_b - 1)^2$ (Talamini et al., 2018), wherein E_b represents the stiffness of the chain segments.

The trends in the normalized force and bond stretch in the chain are plotted against the applied stretch, and juxtaposed with the plot for a rigid chain segment in Fig. 2. In contrast to the classical rigid chain segments model, the force in the elastic chain models does not tend to infinity instantly as the normalized applied stretch $\lambda/\sqrt{N}$ tends to one. This enables the model to capture the response of the material for larger stretches. However, the canonical expression assumed by Mao et al. (2017) exhibits a decrease in the force of the chain after a certain threshold of the applied stretch, which posed an issue in the convergence of our numerical implementation. The expression assumed by Talamini et al. (2018) results in a gradually increasing force with applied stretch, which made it a perfect choice for this study. Hence, we assume the expression of the internal energy due to bond stretch to be

$$\varepsilon_b(\lambda_b) = \frac{1}{2} E_b (\lambda_b - 1)^2 \,. \tag{8}$$

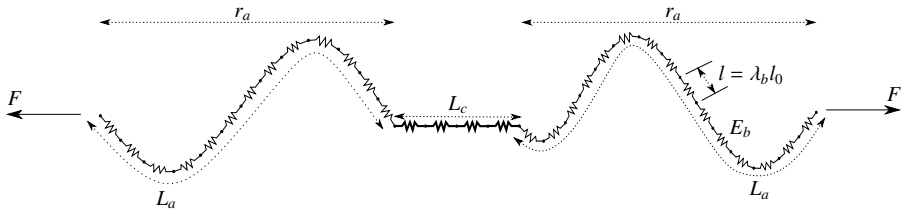

Figure 3: Chain model for semi-crystalline chain with elastic segments

2.2. *Microscopic description for crystallizing rubber*

In contrast to polymer chains in non-crystallizable rubbers, chains in crystallizable rubbers contain both amorphous and crystalline parts when stretched. The amorphous part can be modeled identical to the polymer chains in non-crystallizable rubbers. Crystallization, which is a result of the ordering of polymer chains, can be assumed to have a negligible effect on the intra-molecular structure of the monomers. Considering a negligible effect of crystallization on the intra-segment stiffness, the crystallized segments are also modeled with the same elastic bond stiffness as their amorphous counterparts. This results in a common chain segment model for the entire crystallized chain. The inter-molecular rigidity caused due to the ordering of the chains is accounted for in the fracture criterion in Section 3.2.

A simplistic model of a partially crystallized chain as shown in Fig. 3 is considered, in which the crystalline part is assumed to be along the line joining the ends of the chain. Without loss of generality, the amorphous parts on either side of the crystallized part are assumed to be of equal lengths in accordance with Rastak and Linder (2018). The degree of crystallinity (DOC) in the chain is defined as $\omega = N_c/N$, where N is the total number of segments and N_c is the number of segments that have crystallized. As a common elastic bond stiffness is assumed for both the amorphous and crystalline parts, the length of crystallized part and the total contour length of the chain are given by $L_c = N_c l = N_c \lambda_b l_0$ and $L = Nl = N\lambda_b l_0$, respectively. This results in the equation

$$\omega = \frac{N_c}{N} = \frac{L_c}{L}\,. \tag{9}$$

By defining the effective end-to-end length r_a and the contour length L_a of the amorphous half-parts as $r_a = (r - L_c)/2$ and $L_a = (L - L_c)/2$, the Langevin parameters can be written as

$$\Lambda = \mathcal{L}(\beta) = \frac{r_a}{L_a} = \frac{r - L_c}{L - L_c} = \frac{\lambda/(\lambda_b\sqrt{N}) - \omega}{1 - \omega}\,. \tag{10}$$

Using the expression for the force F given by (2), the free energy of a partially crystallized chain can be derived as

$$\begin{aligned}\psi(\lambda, \lambda_b, \omega) &= \psi_b(\lambda_b) + \int_0^r F^\star \mathrm{d}r^\star + \psi_c(\omega) \\ &= N\varepsilon_b(\lambda_b) + k_B T N(1-\omega)\left(\beta\Lambda + \ln\frac{\beta}{\sinh\beta}\right) + \psi_c(\omega)\,.\end{aligned} \tag{11}$$

Next, the free energy contribution due to crystallization is adapted from Rastak and Linder (2018) and is expressed as

$$\psi_c(\omega) = \tilde{c}\;\omega - \xi\left(\frac{\omega}{\omega_{\max}} + \ln(1 - \frac{\omega}{\omega_{\max}})\right)\,. \tag{12}$$

In the above equation, the first term is related to the energy of fusion and the interface energy of the crystalline phase. The second term bounds the crystallinity to $\omega_{\max}$ due to the effect of entanglements, by penalizing higher values of ω using the penalty parameter ξ. In this study, the effects of loading condition and the initial orientation of the chains are considered on the crystalline interface energy.

Similar to the non-crystallizing case, the argument that bond stretch in the chain segments minimizes the free energy of the chain for a given constant chain stretch and degree of crystallization, is utilized for calculating its value.

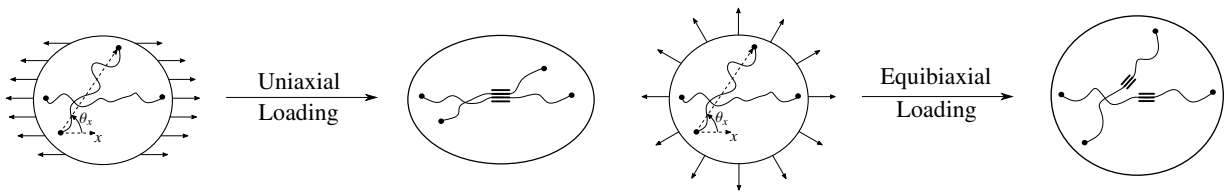

Figure 4: Depiction of the crystallite directions for uniaxial and equibiaxial loading cases assumed for this model based on the experimental findings of Beurrot et al. (2011).

Using the expression for the internal energy due to bond stretch $\varepsilon_b(\lambda_b)$ as in (8), the implicit nonlinear expression for the amount of bond stretch in the chain segments λ_b can be derived as

$$\frac{\partial \psi}{\partial \lambda_b} = 0 \implies E_b\,(\lambda_b - 1)\,\lambda_b^2 = k_B T \frac{\lambda}{\sqrt{N}}\beta\,. \tag{13}$$

The force in the chain due to its stretch is given by

$$f = \frac{\partial \psi}{\partial \lambda} = k_B T \sqrt{N}\frac{\beta}{\lambda_b}\,. \tag{14}$$

The effect of crystallization on force in the chain is reflected by a change in the Langevin parameter β. Similar to the force due to stretch, a driving force indicating the inclination for crystallization at a given state can also be defined as

$$f_w = -\frac{\partial \psi}{\partial \omega} = k_B T N \left(\beta + \ln\frac{\beta}{\sinh\beta}\right) - \tilde{c} - \frac{\xi\omega}{\omega_{\max}\,(\omega_{\max} - \omega)}\,. \tag{15}$$

By following Rastak and Linder (2018), a phenomenological simple linear expression for the rate of crystallization $\dot{\omega}$ is assumed as

$$\dot{\omega} = q f_w \quad \text{with} \quad q \geq 0\,. \tag{16}$$

Since crystallization starts when $\dot{\omega} > 0$, the term $\tilde{c}$ in (15) represents a nucleation barrier. The depiction of the crystallite directions for uniaxial and equibiaxial loading conditions assumed for this model based on the observations of Beurrot et al. (2011) is presented in Fig. 4. In Beurrot et al. (2011), it was found that equibiaxial deformation led to an isotropic crystallization. Other biaxial deformations led to a mean alignment of the crystallites along the first principal loading direction, with a higher degree of disorientation as compared to the uniaxial case.

Firstly, it can be observed from Fig. 4 that the chains along different directions congregate together for forming the crystal during uniaxial loading, while there is a competition for crystallite direction for the case of biaxial loading. Thus, the nucleation barrier for the case of biaxial loading can be assumed to be larger than that for the uniaxial case. Secondly, the nucleation barrier can be assumed to be the same for chains along all directions for the case of equibiaxial loading. However, the nucleation barrier for chains that are nearly perpendicular to the uniaxial loading direction can be assumed to be very high. These effects are accounted for by assuming an empirical expression for $\tilde{c}$ as

$$\tilde{c}\,(\chi, \hat{\boldsymbol{v}}, \boldsymbol{\lambda}_0) = \frac{c}{\left[\sum_{i=1}^{3} \chi_i^2 \left(\sin^{-1} \mid \hat{\boldsymbol{v}}_i \cdot \boldsymbol{\lambda}_0 \mid\right)^{\chi_2/\chi_1} + \gamma\right]^{p_c}}\,. \tag{17}$$

In the above expression, $\tilde{c}$ is considered as a function of the loading condition variables $(\chi, \hat{\boldsymbol{v}})$ and the initial orientation of the chain $\boldsymbol{\lambda}_0$. γ is a small positive constant for bounding the value of the function, and p_c is a parameter that controls the order of the effects of loading condition and the relative orientation of the chain on its crystallinity, as depicted in Fig. 5. For the case $p_c = 0$, (12) retracts to the crystalline free energy function assumed in Rastak and Linder (2018). For simplifying the model, the deformation gradient at the previous time step $\boldsymbol{F}_n$ is utilized as an approximation of the loading condition, as explained in Section 4. Its singular value decomposition yields the principal stretch directions $\hat{\boldsymbol{v}}$, while the crystalline direction weights χ along the i-th principal stretch direction is calculated using the singular values σ as

$$\chi_i = \frac{\sigma_i}{\sum_{j=1}^{3} \sigma_j}\,. \tag{18}$$

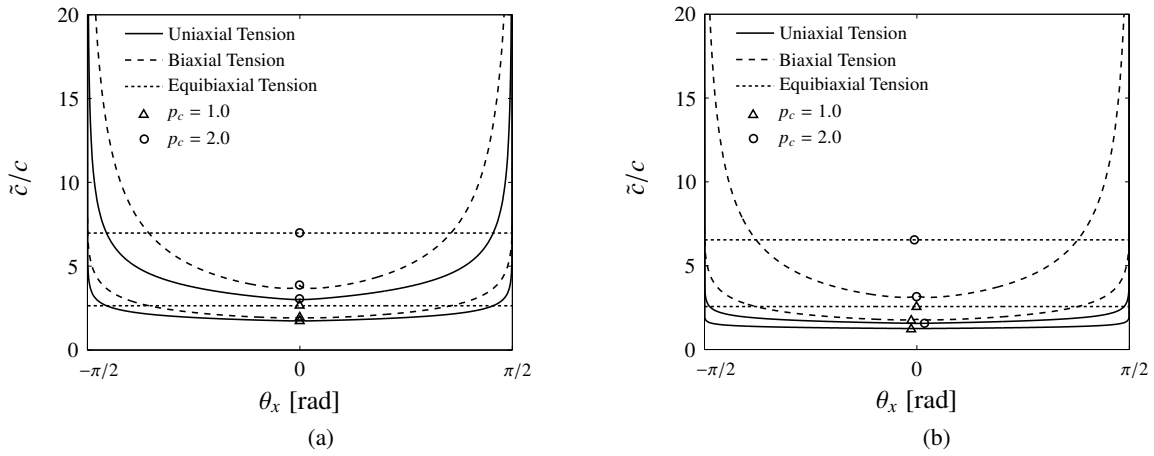

Figure 5: Visualization of the effects of loading condition and material parameter p_c on $\tilde{c}/c$ for chains in the XY plane making an angle θ_x with the X-axis. The loading conditions considered are: (1) $\boldsymbol{F}_{\text{uniaxial}} = \bar{\lambda}\,\boldsymbol{e}_1\otimes\boldsymbol{e}_1 + \bar{\lambda}^{-1/2}\,\boldsymbol{e}_2\otimes\boldsymbol{e}_2 + \bar{\lambda}^{-1/2}\,\boldsymbol{e}_3\otimes\boldsymbol{e}_3$; (2) $\boldsymbol{F}_{\text{biaxial}} = \bar{\lambda}\,\boldsymbol{e}_1\otimes\boldsymbol{e}_1 + \bar{\lambda}/2\,\boldsymbol{e}_2\otimes\boldsymbol{e}_2 + 2\bar{\lambda}^{-2}\,\boldsymbol{e}_3\otimes\boldsymbol{e}_3$; (3) $\boldsymbol{F}_{\text{equibiaxial}} = \bar{\lambda}\,\boldsymbol{e}_1\otimes\boldsymbol{e}_1 + \bar{\lambda}\,\boldsymbol{e}_2\otimes\boldsymbol{e}_2 + \bar{\lambda}^{-2}\,\boldsymbol{e}_3\otimes\boldsymbol{e}_3$. Comparison is made for the cases (a) $\bar{\lambda} = 3.0$ and (b) $\bar{\lambda} = 6.0$.

In (17), the χ^2 term accounts for the increased nucleation barrier for biaxial loading as compared to uniaxial loading. The term $|\,\hat{\boldsymbol{v}}\cdot\boldsymbol{\lambda}_0\,|$ considers the effect of the relative orientation of the chain with respect to the principal loading directions. The sine inverse function results in an equal nucleation barrier for the case of equibiaxial loading. The ratio χ_2/χ_1 represents the uniaxiality of the loading. As chains along different initial orientation are stretched along the same principal stretch direction during uniaxial loading, the effect of the relative orientation is reduced by this ratio.

The visualization of the effects of loading condition and material parameter p_c on the normalized barrier function $\tilde{c}/c$ for chains in the XY plane making an angle θ_x with the X-axis is shown in Fig. 5. The loading conditions considered are: (1) $\boldsymbol{F}_{\text{uniaxial}} = \bar{\lambda}\,\boldsymbol{e}_1\otimes\boldsymbol{e}_1 + \bar{\lambda}^{-1/2}\,\boldsymbol{e}_2\otimes\boldsymbol{e}_2 + \bar{\lambda}^{-1/2}\,\boldsymbol{e}_3\otimes\boldsymbol{e}_3$; (2) $\boldsymbol{F}_{\text{biaxial}} = \bar{\lambda}\,\boldsymbol{e}_1\otimes\boldsymbol{e}_1 + \bar{\lambda}/2\,\boldsymbol{e}_2\otimes\boldsymbol{e}_2 + 2\bar{\lambda}^{-2}\,\boldsymbol{e}_3\otimes\boldsymbol{e}_3$; (3) $\boldsymbol{F}_{\text{equibiaxial}} = \bar{\lambda}\,\boldsymbol{e}_1\otimes\boldsymbol{e}_1 + \bar{\lambda}\,\boldsymbol{e}_2\otimes\boldsymbol{e}_2 + \bar{\lambda}^{-2}\,\boldsymbol{e}_3\otimes\boldsymbol{e}_3$, where we consider $\{\boldsymbol{e}_1, \boldsymbol{e}_2, \boldsymbol{e}_3\}$ as the orthonormal basis to identify positions in both, the reference and the current configurations. As depicted in Fig. 5a, the model predicts a constant barrier $\tilde{c}$ for the equibiaxial case as the crystallite can orient along all the directions with equal probability. For the other two cases, as the tendency of crystallites to form along the first principal stretch direction (X-axis) is higher, $\tilde{c}$ is lower near $\theta_x = 0$ and increases for higher angles. For most of the domain, $\tilde{c}$ can be observed to be smaller for the uniaxial case in comparison with the biaxial case due to the reduced competition for the crystallite directions. As the applied stretch increases for the uniaxial case, more chains along different initial directions are stretched along the principal loading direction. As a result, the additional interface energy needed for the formation of the crystalline phase reduces. This is evident from Fig. 5b. The decrease in $\tilde{c}$ with increased applied stretch for the biaxial case is smaller due to the higher competition for crystallite directions. Moreover, for the case of equibiaxial tension, the model predicts a very small change in $\tilde{c}$ for higher applied stretches.

Assuming the density of chains per unit volume as n, the normalized chain thermodynamic variables are defined as

$$\bar{\psi} = n\psi\,, \quad \bar{f} = nf\,, \quad \bar{f}_w = nf_w \tag{19}$$

which are as described in Rastak and Linder (2018). Similarly, the normalized chain parameters can be denoted as

$$\mu = nk_BT\,, \quad E = nE_b\,, \quad \bar{c} = nc\,, \quad \bar{\xi} = n\xi\,, \quad \bar{q} = \frac{q}{n}\,. \tag{20}$$

Remark 1. In this study, the crystalline parts are modeled to have a similar elastic bond stiffness as the amorphous parts. An alternative approach is to include the rigidity of the crystallites in the elastic stiffness E_b itself leading to an *effective* bond stretch. This would result in different elastic stiffness values for the amorphous and crystalline parts, which would in turn result in an involved formulation. Accounting for the increase in the rigidity due to the increase in inter-molecular attractions with crystallization would further complicate it. The paucity in experiments measuring the

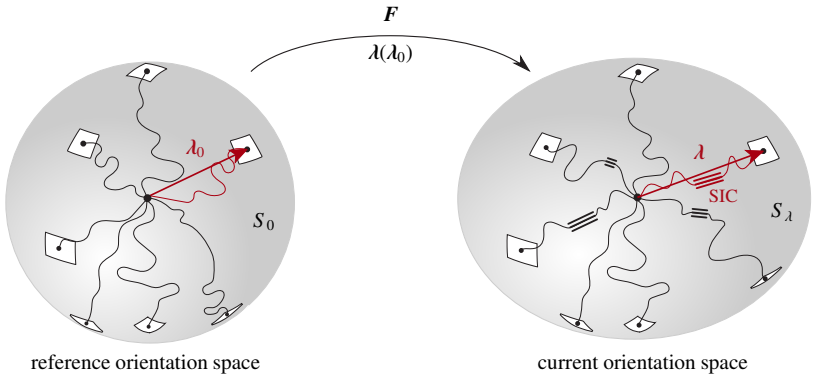

Figure 6: Depiction of the reference and current orientation spaces of a unit volume of material wherein chains along discrete quadrature directions are considered for numerical purposes.

relative rigidity of the crystalline portions as compared to the amorphous segments further exacerbates the problem. Thus, this study has adopted the method of modeling the internal bond energy of the crystalline segments similar to the amorphous parts, keeping in mind the physical and numerical aspects of the problem.

So far, the physical properties of polymer chains have been studied at the microscopic scale where each chain has been modeled as a one-dimensional entity described by its micro-mechanical variables such as stretch, degree of crystallinity, and covalent bond stretch. The primary goal of the following two sections is to define the macroscopic behavior of the material and to mathematically connect it with the microscopic description of polymer chains within a vast random network.

2.3. Bridging micro- and macroscopic deformation

In the macroscopic setting, a large deformation framework is used for capturing the behavior of rubber-like materials due to their high stretchability. Owing to their incompressible response, a decoupled deformation gradient approach (Flory, 1961) is adopted in this study. The deformation gradient $\boldsymbol{F}$ can be decomposed multiplicatively into volumetric $\boldsymbol{F}_{\text{vol}}$ and isochoric $\bar{\boldsymbol{F}}$ components as

$$\boldsymbol{F} = \boldsymbol{F}_{\text{vol}}\bar{\boldsymbol{F}} \quad \text{where} \quad \boldsymbol{F}_{\text{vol}} = J^{1/3}\boldsymbol{I}, \quad \bar{\boldsymbol{F}} = J^{-1/3}\boldsymbol{F}, \quad J = \det\boldsymbol{F} > 0\,. \tag{21}$$

The crystallization phenomenon is assumed to affect only the isochoric part of the free energy. This macroscopic description of deformation of the body should be linked to the deformation of polymer chains in the microscopic setting, using an appropriate model accounting for the kinematic compatibility. The following explanation is based on Rastak and Linder (2018) and briefly encompasses the utilization of network homogenization based on the maximal advance path constraint model (Tkachuk and Linder, 2012) in conjunction with the principle of minimum average free energy for achieving the connection.

In the previous sections, polymer chains were modeled to resist deformation with the help of their one-dimensional tensile stiffness. As there are a large number of polymer chains oriented along different directions, tracking their individual behavior for a given external loading is infeasible. This necessitates homogenizing the network of chains by means of a few simplifying assumptions.

One such homogenization method considers all the chains oriented along a particular direction $\boldsymbol{\lambda}_0$ in the reference configuration to have similar properties like stretch, internal force, bond stretch and degree of crystallization. The reference orientation vector can be calculated as $\boldsymbol{\lambda}_0 = \boldsymbol{r}_0/|\boldsymbol{r}_0|$, where $\boldsymbol{r}_0$ is the end-to-end vector of a chain in its undeformed state. This assumption simplifies the behavior of chains in a material to be a function of only their reference orientations, while all other parameters like length, stiffness and number of segments are considered uniform across all chains. This means that if two polymer chains are oriented parallel to each other in the initial network configuration, they are assumed to behave identically throughout any deformation or change of phase. The assumption is in line with those adopted by Wu and Van Der Giessen (1993), Miehe et al. (2004), Kroon (2010), or Tkachuk and Linder (2012). Rubber's isotropic behavior in the undeformed configuration makes it reasonable to assume a uniform distribution

of polymer chains along all reference orientations. Thus, each reference orientation can be mapped onto a point on the surface of a unit sphere called reference orientation space, which simplifies the study of the response of random networks in a statistical manner.

In the actual configuration, due to different chain properties along different reference orientations, the orientation space forms an ellipsoid. However, the assumption that these properties depend only on the reference orientation of the polymer chain can be utilized for performing statistical operations on the unit spherical reference orientation space. Let $\boldsymbol{\lambda} = \boldsymbol{r}/|\boldsymbol{r}_0|$ represent the stretch vector in each chain, where $\boldsymbol{r}$ represents the chain end-to-end vector in the deformed configuration. The isochoric part of the macroscopic free energy in the deformed configuration $\bar{\Psi}$ can be obtained by averaging the free energies in all the chains using the reference orientation space, while assuming a negligible contribution by the crosslink points. A numerical integration scheme for symmetric functions over the unit sphere proposed by Bažant and Oh (1986) is utilized for computing the averaged quantities in the reference orientation space as

$$\bar{\Psi} = \langle \bar{\psi}\left(\lambda, \lambda_b, \omega\right) \rangle = \sum_{l=1}^{n_{\text{int}}} \bar{\psi}\left(\lambda_l, \lambda_{b,l}, \omega_l\right) W_l \tag{22}$$

where λ_l, $\lambda_{b,l}$, ω_l and W_l are the stretch, bond stretch, degree of crystallization and the weight coefficient, respectively, for the chains directed along the l-th quadrature orientation $\boldsymbol{\lambda}_{0,l}$ in the undeformed configuration, and n_{int} refers to the number of quadrature directions.

Although the chain network can deform and transform in many different ways, the chains should maintain kinematic compatibility with each other and with the macroscopically observable deformation tensor $\bar{\boldsymbol{F}}$. In the affine deformation model (Wu and Van Der Giessen, 1993), the stretch vector in the deformed configuration is assumed to be mapped to the undeformed orientation by $\boldsymbol{\lambda} = \bar{\boldsymbol{F}}\boldsymbol{\lambda}_0$. As the strong local constraints limit the flexibility of the network and lead to a stiff response of the rubber model, a non-affine model called maximal advance path constraint is used. In this model, specific paths formed by connected chains that have the maximal advance in a certain direction are called the maximal advance paths. The end-to-end vectors of these maximal advance paths that are long enough to reach the macroscopic scales of the continuous body are postulated to undergo an affine deformation (Tkachuk and Linder, 2012). This constraint depends on the number of chains connected at each crosslink point, known as the network functionality. Assuming it to be four, the compatibility equation can be written as

$$\langle \boldsymbol{\lambda} \otimes \boldsymbol{\lambda}_0 \rangle = \sum_{l=1}^{n_{\text{int}}} \left(\boldsymbol{\lambda}_l \otimes \boldsymbol{\lambda}_{0,l}\right) W_l = \tfrac{1}{3}\, \bar{\boldsymbol{F}}\,. \tag{23}$$

However, the set of micromechanical constraints does not uniquely identify a single possible network response, but rather specifies a space of possible configurations. The constraint (23) results in an infinite space of solution set due to the internal degrees of freedom of the freely rotating chain segments. In order to provide a constitutive model at the macroscale, we have to choose one unique configuration out of all possible states. This can be done by minimizing the free energy of the network using the principle of minimum average free energy for random networks (Miehe et al., 2004), and finding the corresponding stretch and orientation of the chains using

$$\boldsymbol{\lambda} = \underset{\boldsymbol{\lambda}}{\operatorname{argmin}}\, \bar{\Psi} = \underset{\boldsymbol{\lambda}}{\operatorname{argmin}}\, \langle \bar{\psi} \rangle \ . \tag{24}$$

Using (23) and (24), the constrained optimization problem can be formulated as

$$\underset{\boldsymbol{\lambda}}{\text{Minimize}}\ \langle \bar{\psi} \rangle \ \text{ subject to } \langle \boldsymbol{\lambda} \otimes \boldsymbol{\lambda}_0 \rangle = \tfrac{1}{3}\, \bar{\boldsymbol{F}}\,. \tag{25}$$

Solving this problem, as done in Tkachuk and Linder (2012), the deviatoric stress tensor can be obtained as

$$\bar{\boldsymbol{P}} = \frac{\partial \bar{\Psi}}{\partial \bar{\boldsymbol{F}}} = \left\langle \bar{\boldsymbol{f}} \otimes \boldsymbol{\lambda}_0 \right\rangle \tag{26}$$

where the normalized force vector $\bar{\boldsymbol{f}}$ has the magnitude of $\bar{f}$ and is along the direction of $\boldsymbol{\lambda}$. This equation is further utilized during the numerical implementation of the algorithm in Section 4. The main advantages of this model are that this constraint overcomes the high rigidity of the affine models by minimization of the free energy and accounts for the anisotropic behavior of the stretched network.

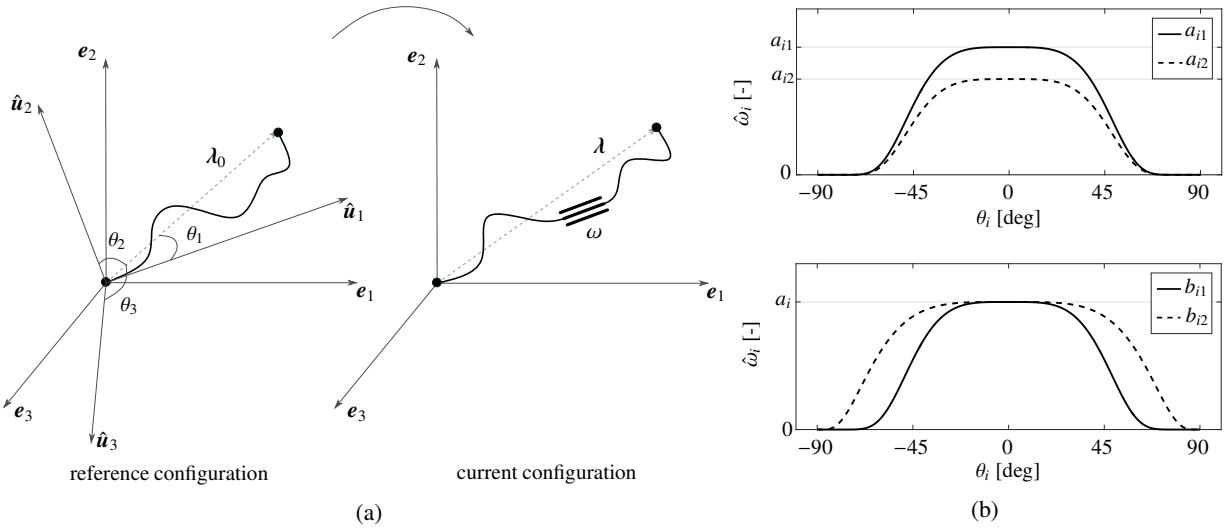

Figure 7: Depiction of the macroscopic crystallinity distribution framework used in our study. (a) Angles θ_i made by a chain oriented along $\boldsymbol{\lambda}_0$ in the reference configuration, with the principal distribution directions $\hat{\boldsymbol{u}}_i$; (b) Illustration of the individual crystallinity distributions $\hat{\omega}_i$ centered around $\hat{\boldsymbol{u}}_i$ for different values of θ_i, and the depiction of the physical significance of the distribution variables a_i and b_i, with $a_{i1} > a_{i2}$, $b_{i1} > b_{i2}$.

2.4. Bridging micro- and macroscopic crystallinity

In Rastak and Linder (2018), uniaxial loading was implicitly assumed and a continuous crystallinity distribution function about a principal crystallite direction, which is close to the uniaxial stretch direction, is adopted in order to overcome the large memory requirement for tracking discrete crystallinity along each quadrature direction. As a simple extension to multiaxial cases, principal crystallinity distribution directions $\hat{\boldsymbol{u}}$ are assumed close to the principal stretch directions $\hat{\boldsymbol{v}}$ and the same distribution function $\hat{\omega}$ is assumed along each of these directions. Finally, the degree of crystallization in each chain is calculated as a simple linear combination of these distributions weighted by the crystallinity direction weights χ and can be written as

$$\omega\left(\boldsymbol{\Omega}, \chi, \boldsymbol{\lambda_0}\right) = \sum_{i=1}^{n_{\text{crys}}} \chi_i \hat{\omega}_i = \sum_{i=1}^{n_{\text{crys}}} \chi_i \; a_i \exp\left(-b_i (\ln \cos\theta_i)^2\right) \quad \text{with} \quad \cos\theta_i = |\, \hat{\boldsymbol{u}}_i(\phi_{1i}, \phi_{2i}) \cdot \boldsymbol{\lambda_0} \,| \; . \tag{27}$$

Remark 2. Note that this simple decoupled linear combination is reasonable as the effects of multiaxial loading have been accounted for in the microscopic chain model itself. Also, the principal distribution directions do not refer to the only orientations that the crystallites can take. However, the first principal distribution direction is always one of the preferred directions. Additionally, Beurrot et al. (2011) have qualitatively reported a range of orientations the crystallites align along, depending on the biaxiality of the applied loading. However, more quantitative experimental studies are required to make a concrete claim regarding their orientations during biaxial loading.

In the above equation, $\boldsymbol{\Omega}_i = (\phi_{1i}, \phi_{2i}, a_i, b_i)$ represents the array of macroscopic crystallinity internal variables along the i-th principal distribution direction, wherein ϕ_1 and ϕ_2 are the spherical coordinates representing the orientation of each principal distribution direction, a expresses the intensity of the crystallinity distribution and b serves as a measure of the spread of crystallinity distribution among the various orientations, as illustrated in Fig. 7b. The unit vector $\hat{\boldsymbol{u}}$ points along each principal distribution orientation as depicted in Fig. 7. Without loss in generalization, assuming the Z-axis to be the reference axis, the unit vector $\hat{\boldsymbol{u}}$ along the i-th principal distribution direction is given as

$$\hat{\boldsymbol{u}}_i = \sin\phi_{1i}\cos\phi_{2i}\; \boldsymbol{e}_1 + \sin\phi_{1i}\sin\phi_{2i}\; \boldsymbol{e}_2 + \cos\phi_{1i}\; \boldsymbol{e}_3 \; . \tag{28}$$

The efficacy of the macroscopic crystallinity model represented by (27) is studied in Appendix B by visualizing it for different loading cases. Furthermore, the apparent rate of crystallization assuming this distribution can be calculated as

$$\tilde{\omega} = \frac{\partial}{\partial t}\omega\left(\boldsymbol{\Omega}, \chi, \boldsymbol{\lambda_0}\right) = \left[\frac{\partial \omega\left(\boldsymbol{\Omega}, \chi, \boldsymbol{\lambda_0}\right)}{\partial \boldsymbol{\Omega}}\right]^T \left[\frac{\partial \boldsymbol{\Omega}}{\partial t}\right] . \tag{29}$$

In this model, the effect of the time dependence of χ, which is calculated using the deformation gradient at the previous time step $\boldsymbol{F}_n$ as explained in Section 4, is neglected as a simplifying assumption. However, the true rate of crystallization is calculated using the microscopic chain properties and is given by (16). For compatibility, the value of the rate of macroscopic crystallinity $\partial\boldsymbol{\Omega}/\partial t$ should minimize the error between the true and apparent crystallization rates and can be obtained by solving the least square problem as

$$\frac{\partial\boldsymbol{\Omega}}{\partial t} = \underset{\partial\boldsymbol{\Omega}/\partial t}{\operatorname{argmin}} \left[\tfrac{1}{2} \left\langle \left(\dot{\omega} - \tilde{\dot{\omega}}\right)^2 \right\rangle + \tfrac{1}{2}\gamma \left[\frac{\partial\boldsymbol{\Omega}}{\partial t}\right]^T \left[\frac{\partial\boldsymbol{\Omega}}{\partial t}\right] \right] . \tag{30}$$

The additional regularization term ensures the convexity of the system for a numerical solution to exist. γ is the regularization constant and is chosen to be a small positive number. The solution for the minimization problem can be obtained as

$$\dot{\boldsymbol{\Omega}} = \mathcal{A}^{-1} \left\langle \dot{\omega} \left[\frac{\partial\omega}{\partial\boldsymbol{\Omega}}\right] \right\rangle \quad \text{where} \quad \mathcal{A} = \left\langle \left[\frac{\partial\omega}{\partial\boldsymbol{\Omega}}\right] \left[\frac{\partial\omega}{\partial\boldsymbol{\Omega}}\right]^T \right\rangle + \gamma \boldsymbol{I}_{4n_{\text{crys}}} . \tag{31}$$

In the above equation, n_{crys} represents the number of contributing distribution directions, $\boldsymbol{I}_{4n_{\text{crys}}}$ is the $4n_{\text{crys}} \times 4n_{\text{crys}}$ identity matrix and $\partial\omega/\partial\boldsymbol{\Omega}$ is the crystallinity gradient array. The evolution equation of the macroscopic crystallinity variables given by (31) can be utilized to compute the crystallinity distributions at each step and this is numerically achieved using the steps described in Section 4.2.

As it is infeasible to experimentally measure the degree of crystallization ω in each chain, we consider a macroscopic variable called crystallinity ratio $\bar{\omega}$. Physically, this represents the mass or volume ratio of the crystallized regions in the whole body. Experimentally, this is calculated by measuring the X-ray diffraction intensity at various angles and then performing a numerical integration as explained in Toki et al. (2003). Similar to Rastak and Linder (2018), this model assumes $\bar{\omega}$ to be proportional to the average ω across all chains and is given by

$$\bar{\omega} = \alpha \langle\omega\rangle = \alpha \sum_{l=1}^{n_{\text{int}}} \omega_l W_l , \tag{32}$$

wherein the proportionality factor α takes into account the inconsistencies between the experimental measurements and theoretical assumptions. It is calibrated as a material parameter.

3. Fracture initiation criterion

Motivated by the study of Lake and Thomas (1967), an approach for postulating the fracture initiation criterion for a polymer based on the condition for the scission of its chains is followed by Mao et al. (2017). A segment can be assumed to have failed if the internal energy due to the bond stretch overcomes the binding energy of the bonds. This critical energy of bond dissociation can be denoted by ε_b^f. Lake and Thomas (1967) state that the amount of internal energy required to rupture a chain having N monomers would then be $N\varepsilon_b^f$ due to the averaging while force gets transmitted through the crosslinks. Using this knowledge, the fracture criterion proposed by Mao et al. (2017) is combined with the MAPC model and extended to crystallizing rubbers in this work.

3.1. Non-crystallizing rubber

For non-crystallizing rubbers, the interaction between the polymer chains can be assumed to be negligible and hence the critical internal energy can be bereft of the effects of van der Waal's forces and even bond angle rotations. So, scaling the chain scission condition to the macroscopic level, the critical internal energy for the chain scission of a unit volume of the material can be written as

$$\varepsilon_{\text{cr}}^f = nN\varepsilon_b^f . \tag{33}$$

Considering the fact that fracture is size-dependent, length scale plays a vital role in this phenomenon. According to Thomas (1955), this length scale can be approximated using the critical energy release rate G_c and the critical total free energy density $\bar{\Psi}_{\text{cr}}^f$ at the crack propagation point as

$$\ell \simeq G_c/\bar{\Psi}_{\text{cr}}^f \simeq G_c/\varepsilon_{\text{cr}}^f . \tag{34}$$

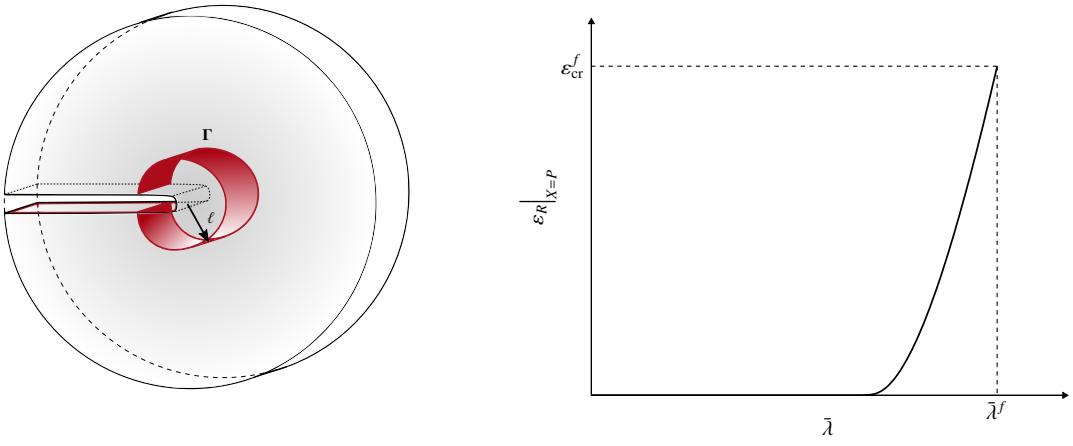

(a) (b)

Figure 8: Depiction of the fracture initiation criterion. (a) Location of surface $\mathbf{\Gamma}$ at a distance of ℓ from the notch root in the reference configuration. The point on this surface in 3D where the internal bond energy for rupture ε_R is maximum is denoted as P. (b) Representative plot of internal bond energy for rupture at point P, $\varepsilon_R\big|_{X=P}$, with applied stretch $\bar{\lambda}$. When $\varepsilon_R\big|_{X=P} = \varepsilon_{\rm cr}^f$, fracture initiation is postulated to occur at stretch $\bar{\lambda}^f$.

In the above equation, the critical total free energy density can be approximated by the critical internal energy because of the negligible contribution by the other free energies at the point of rupture. As an extension of the criterion proposed by Mao et al. (2017) to multiaxial cases, the possibility of crack emanating at any angle should be considered. For achieving this, a surface $\mathbf{\Gamma}$ in 3D can be considered at a distance ℓ from the notch root in the reference configuration, as illustrated in Fig. 8. The point on this surface where the internal bond energy to rupture ε_R is the maximum, can be denoted as P. As postulated in Mao et al. (2017), the fracture initiation can be assumed to occur when the critical value of internal energy due to bond distortion is reached at point P. In other words,

$$\varepsilon_R\Big|_{X=P} = \varepsilon_{\rm cr}^f \implies \text{fracture initiation}\,. \tag{35}$$

Mao et al. (2017) adapted the eight-chain network model developed by Arruda and Boyce (1993) by considering an effective distortional stretch in each of the eight representative chains along the diagonals of a unit cube. The resulting effective bond stretch value in each chain was utilized to calculate the internal bond stretch energy for rupture ε_R. However, chains along the direction of external load are known to stretch more than those in other configurations. This anisotropy is not captured by this model and therefore the maximum bond stretch energy in those chains which are responsible for the fracture initiation are not always considered.

As explained in the previous section, the MAPC model accounts for the anisotropy in the polymer network system. As a result, the stretches in the chains along different initial orientations can be obtained uniquely. Whenever the chains with the maximum internal bond stretch energy reach the criterion (35), chain scission occurs and they shift the responsibility of load-carrying to the remaining chains. As this triggers the rupture of the whole network system, this event is considered as the fracture initiation point. During experiments, since it is approximately measured as the point when the crack starts to propagate, this point is also referred to as the crack initiation point. Thus, the internal bond stretch energy for rupture can be expressed as

$$\varepsilon_R = \max_{l=1,\ldots,n_{\rm int}} nN\varepsilon_b\left(\lambda_{b,l}\right)\,. \tag{36}$$

In the above equation, $\lambda_{b,l}$ represents the bond stretch in the chains initially oriented along the l-th integration direction. A comparison study of this model with that developed by Mao et al. (2017) using the eight-chain network model has been presented in Appendix D and it shows the conservativeness of this model. Besides this, the physical significance of the criterion is another major advantage of this model.

3.2. Crystallizing rubber

In Section 2.2, the rigidity of the crystalline portions were not accounted for in modeling the chain segments as they were categorized as inter-molecular forces. Consequently, the assumption for non-crystallizing rubbers that the inter-chain interactions can be neglected does not hold true for the case of crystallizing rubbers for formulating the fracture criterion. To account for the physicality in the model, we delve into the study of the physical structure and evolution of the crystallites. Experimental studies by Trabelsi et al. (2003) and Che et al. (2013) found that the major increase in the crystallinity fraction was due to the increase in the number of crystallites with stretch. They found the volume of each crystallite to be nearly constant at low temperatures of -25°C and -50°C, respectively. However, studies by Candau et al. (2014) and Chenal et al. (2007) at room temperature found the crystallite sizes in the lateral direction to the uniaxial load to increase with the applied stretch, even though the size along the longitudinal direction had negligible effect. This observation would be incorporated in the formulation of the critical energy for crack initiation.

The critical energy required for dissociating the atomistic bonds of the chains can be taken from the previous part as

$$\varepsilon^f_{\text{bond}} = nN\varepsilon^f_b \,. \tag{37}$$

However, it has been noted in Hamed (1994) that the distortion of crystallites precedes the rupture of the chains. Thus, energy must be spent in breaking through the crystallite for rupture. For simplicity, let us assume that the crystallite distortional energy is a linear function of the critical bond dissociation energy as

$$\varepsilon^f_{\text{crystal}} = R(\omega)\, \varepsilon^f_{\text{bond}} \,. \tag{38}$$

The function $R(\omega)$ in the above equation can be attributed to be a measure of the rigidity of the crystal structure. The lack of experimental findings of the stiffness of the crystallite ushers us to formulate a phenomenological expression for $R(\omega)$. As the fracture initiation criterion using the MAPC model accounts for anisotropy, the chains in a unit volume along a particular initial orientation with the maximum stretch and degree of crystallinity ω can be considered.

It can be clearly noticed that the rigidity is proportional to the amount of crystallization as a higher amount of energy is required to distort a larger total volume of the crystallites. As stated earlier, since the amount of crystallization along those chains is mostly constituted by the number of crystallites, it can be reasonably represented by their ω, considering the lateral sizes as insignificant as compared to the total length of the crystallized chain portion. The effect of the lateral size increase can be attributed to the increase in the spread of crystallization or the interaction between adjoining crystals, which results in an increased density of inter-molecular attractions. In an ideal case, the rigidity should shoot up to a very large value as ω tends to 1, which would signify the high relative rigidity of the crystal structure as compared to the molecular bond strength of monomers. Considering these arguments, the crystallite distortion energy is assumed to have the following form.

$$\varepsilon^f_{\text{crystal}} = \frac{\omega}{1-\omega}\, \varepsilon^f_{\text{bond}} \tag{39}$$

Remark 3. A similar trend has been used by Zhou et al. (2014) for predicting the toughness effect of SIC using a double network structure. Their model consists of a hard domain consisting of crystallites and a soft domain consisting of amorphous chains. The toughness effect for an equal strain case has been modeled as a product of the hard domain volume fraction (which nearly follows the trend of ω) and a cut-off factor (which follows a trend similar to that of $(1-\omega)^{-1}$). Though the arguments were for the case of rubber fracture, similar arguments can be adopted for the prediction of fracture initiation.

The effective critical energy for fracture initiation can be obtained as

$$\varepsilon^f_{\text{cr,eff}} = \varepsilon^f_{\text{bond}} + \varepsilon^f_{\text{crystal}} = \frac{nN\varepsilon^f_b}{1-\omega} = \frac{\varepsilon^f_{\text{cr}}}{1-\omega} \,. \tag{40}$$

The above expression for the critical energy converges to the case of non-crystallizable rubbers for $\omega = 0$. If the amount of crystallization in the chain at rupture is expected to be large for a material, then the amount of energy it has to spend for distorting the crystallite is large. Theoretically, as $\omega \to 1$, $\varepsilon^f_{\text{cr,eff}} \to \infty$ which suggests that the rupture

stretch is very large. But practically, as explained earlier, due to entanglements and effects from neighboring chains, ω in each chain is bounded by the parameter $\omega_{\max} < 1$ in our model. Although the crystal dissociation energy is an increasing function of ω, its property of saturating to $\omega_{\max}$ for higher stretches ensures a finite fracture initiation point.

According to Lake and Thomas (1967), as the bond distortion energy dominates the total free energy of the system at rupture, it is rational to consider mainly the internal energy due to the bond stretching to provide the effective critical energy. The fracture initiation criterion for crystallizing rubbers can be postulated in a similar manner to that for non-crystallizing rubber given by (35) and (36) as

$$\max_{l=1,\ldots,n_{\text{int}}} nN\varepsilon_b\left(\lambda_{b,l}\right)\Big|_{X=P} = \varepsilon^f_{\text{cr,eff}} \implies \text{fracture initiation}\,. \tag{41}$$

Rearranging the terms, the fracture criterion can be rewritten as

$$\max_{l=1,\ldots,n_{\text{int}}} nN\left(1-\omega_l\right)\varepsilon_b\left(\lambda_{b,l}\right)\Big|_{X=P} = \varepsilon^f_{\text{cr}} \implies \text{fracture initiation}\,. \tag{42}$$

The fracture criterion can be put in the same format as that of non-crystallizing rubbers given by (35) as

$$\varepsilon_R\Big|_{X=P} = \varepsilon^f_{\text{cr}} \implies \text{fracture initiation, with} \quad \varepsilon_R = \max_{l=1,\ldots,n_{\text{int}}} nN\left(1-\omega_l\right)\varepsilon_b\left(\lambda_{b,l}\right)\,. \tag{43}$$

The value of the critical energy for chain scission $\varepsilon^f_{\text{cr}}$ is calculated in line with the ab initio calculations performed by Mao et al. (2017). A key feature of this criterion is that it converges to the case of non-crystallizing rubbers for $\omega = 0$ and hence can be uniformly used for both crystallizing and non-crystallizing rubbers.

Remark 4. Even though the length scale ℓ is an intrinsic material parameter, it is chosen based on its dimensions for computational tractability. For the equation (34) to hold, the value of $\varepsilon^f_{\text{cr}}$ is suitably scaled as explained in Talamini et al. (2018). Even for the case of crystallizing rubbers, the approximations $\Psi^f_{\text{cr}} \simeq \varepsilon^f_{\text{cr,eff}}$ (neglecting the additional contribution by crystallization) and $\varepsilon^f_{\text{cr,eff}} \simeq \varepsilon^f_{\text{cr}}$ (considering their order of magnitude for most practical applications wherein the amount of crystallization is not large) can be assumed to roughly hold so as to satisfy (34).

4. Numerical Implementation

Observing the need for solving nonlinear implicit equations to obtain the isochoric components of the Kirchhoff stress tensor $\bar{\boldsymbol{\tau}}$ and the corresponding tangent modulus $\bar{\mathbb{C}}$, the process is accomplished with the help of the Newton-Raphson algorithm. The basic framework followed by Rastak and Linder (2018) is built upon by adding an extra loop for the calculation of the bond stretch λ_b. To simplify the complex algorithm, it can be split up into three main loops, which for our convenience have been named as the Bond Stretch loop, Crystallization loop and the MAPC loop, with each loop encompassing the previous one in the sequence.

The top-down view of the numerical algorithm have been represented by the flow diagrams in Fig. 9 and Fig. 10. In Fig. 9, the outermost loop is shown to obtain the deformation gradient and history variables as inputs. This MAPC loop calls the Crystallization loop within it and finally outputs the stress tensor and the tangent operator. It can be observed that the Crystallization loop in Fig. 10 calls the Bond Stretch loop, which is the innermost loop. With the knowledge of this basic framework, each of the loops are explained in the upcoming subsections in a bottom-up manner for a better understanding.

4.1. Bond Stretch Loop

The bond stretch loop forms the inner-most loop of the algorithm. Given the chain force corresponding to the stretch and the degree of crystallization, the bond stretch in the chain segments in each of the integration orientation is obtained by performing Newton-Raphson iterations as shown in Fig. 10.

With the help of the chain force, the Langevin parameters are calculated in accordance to (14) as

$$\beta = \frac{\bar{f}}{\mu\sqrt{N}}\,, \quad \Lambda = \coth\beta - \beta^{-1}\,. \tag{44}$$

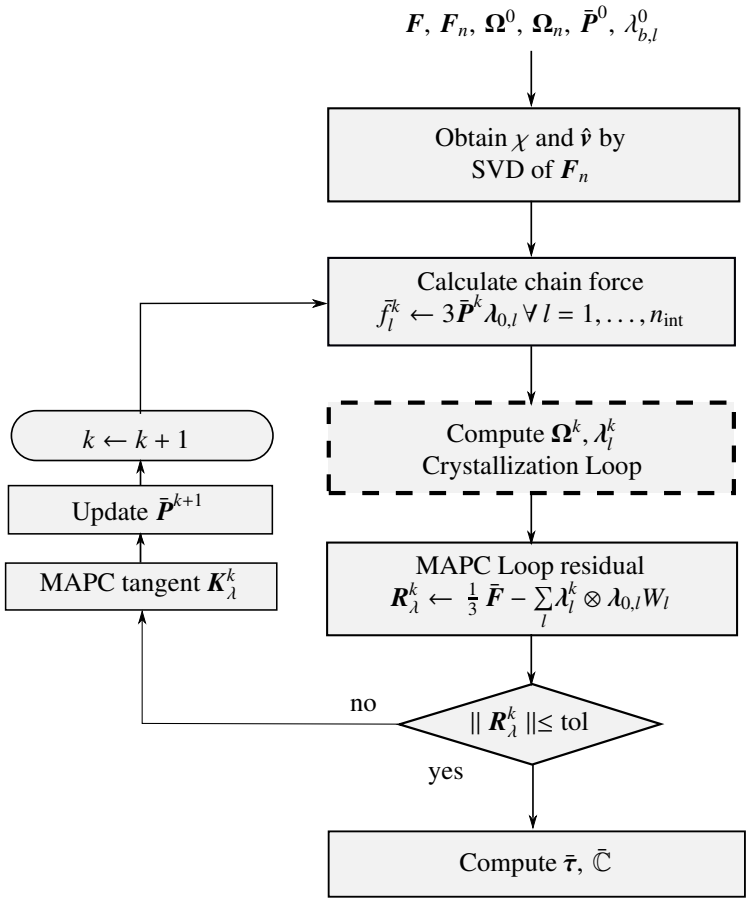

Figure 9: Flow diagram for the MAPC Loop of the numerical algorithm at time t_{n+1}

In addition to these computed Langevin parameters, using an initial guess of the bond stretch and the corresponding degree of crystallization, the current chain force can be calculated similar to (10) as

$$\lambda = \lambda_b \sqrt{N}\,(\omega + (1-\omega)\Lambda)\ . \tag{45}$$

The implicit equation as derived in (13) is used as the residual and iterations are performed till this value goes below a specified tolerance. This tolerance is chosen to optimally minimize the error in the obtained value of λ_b while keeping in mind the accuracy due to computer floating point precision. To minimize the numerical errors as explained in Appendix A, the expression for the residual that was chosen is

$$R_b = -(\lambda_b - 1) + \frac{\mu}{E}\beta\frac{\lambda}{\lambda_b^2\sqrt{N}}\,. \tag{46}$$

For deriving the tangent for the bond stretch loop, the chain force $\bar{f}$ and the degree of crystallization ω are considered to stay constant during the iterations inside this loop. However, the magnitude of chain stretch λ alters with the changing bond stretch λ_b. So, the tangent can be obtained as

$$K_b = -\frac{\mathrm{d}R_b}{\mathrm{d}\lambda_b} = -\frac{\partial R_b}{\partial \lambda_b} - \frac{\partial R_b}{\partial \lambda}\frac{\partial \lambda}{\partial \lambda_b}\bigg|_{\bar{f},\,\omega}\,. \tag{47}$$

The total change in the normalized chain force can be expressed as

$$\mathrm{d}\bar{f} = \frac{\partial \bar{f}}{\partial \lambda}\mathrm{d}\lambda + \frac{\partial \bar{f}}{\partial \lambda_b}\mathrm{d}\lambda_b + \frac{\partial \bar{f}}{\partial \omega}\mathrm{d}\omega = k_{\bar{f}\lambda}\mathrm{d}\lambda + k_{\bar{f}\lambda_b}\mathrm{d}\lambda_b + k_{\bar{f}\omega}\mathrm{d}\omega\,. \tag{48}$$

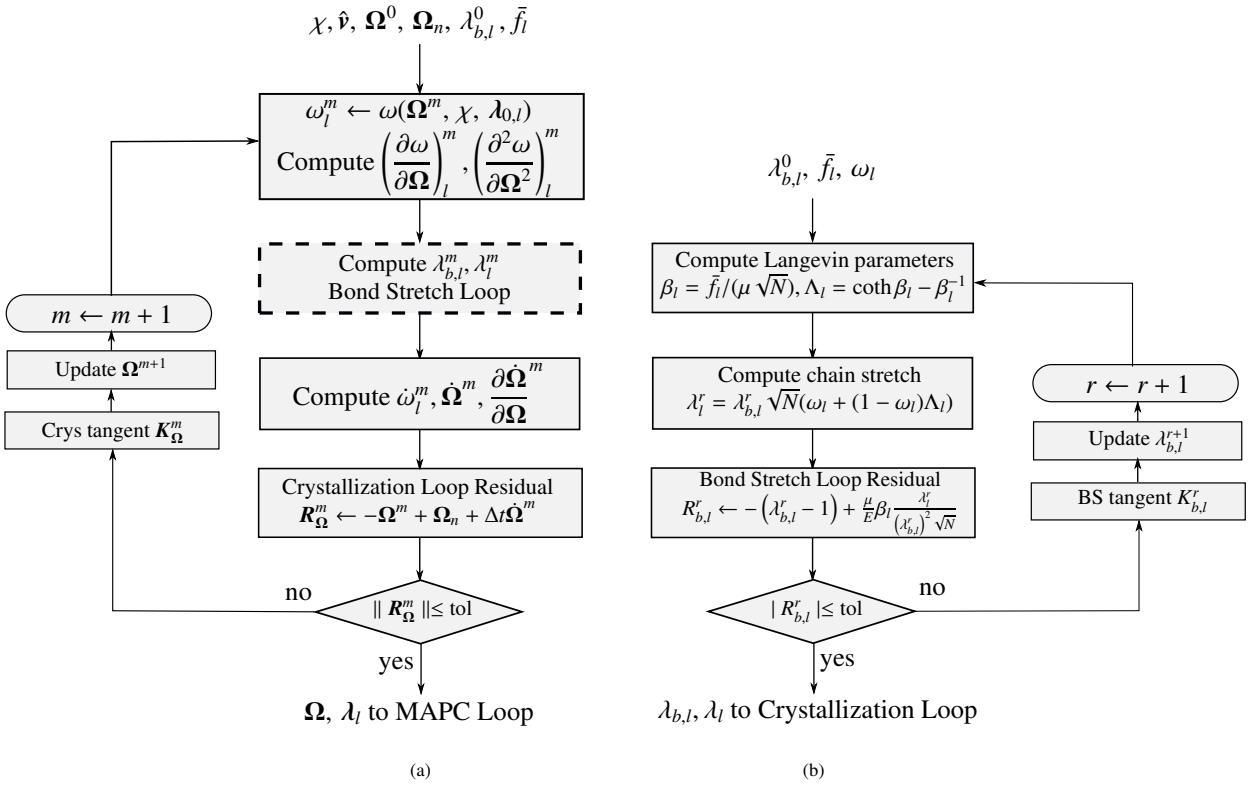

Figure 10: Flow diagram for (a) Crystallization loop and (b) Bond Stretch loop of the numerical algorithm

Mathematically, a constant normalized chain force and degree of crystallization can be expressed as $\mathrm{d}\bar{f} = \mathrm{d}\omega = 0$. Using these in the above expression, it can be written as

$$\left.\frac{\partial\lambda}{\partial\lambda_b}\right|_{\bar{f},\omega} = -\frac{k_{\bar{f}\lambda_b}}{k_{\bar{f}\lambda}}\,. \tag{49}$$

Using the expression for the chain force as given by (14) and the normalization given by (19) and (20), the expressions for $k_{\bar{f}\lambda}$ and $k_{\bar{f}\lambda_b}$ can be derived as

$$k_{\bar{f}\lambda} = \frac{\mu}{\lambda_b^2(1-\omega)\mathcal{L}'(\beta)}\,, \quad k_{\bar{f}\lambda_b} = -\frac{\lambda}{\lambda_b}k_{\bar{f}\lambda} - \frac{\mu\beta\sqrt{N}}{\lambda_b^2}\,. \tag{50}$$

After calculating each of the terms in (47) as shown in Appendix A and simplifying, the expression for the bond stretch tangent can be obtained as

$$K_b = 1 + \frac{\mu}{E}\beta\frac{1}{\lambda_b^2\sqrt{N}}\left(\frac{\lambda}{\lambda_b} + \frac{k_{\bar{f}\lambda_b}}{k_{\bar{f}\lambda}}\right). \tag{51}$$

As this is the loop that is run the most, it is vital that the convergence is the fastest. An initial guess of $\lambda_b = 1$ for all the integration orientations results in the convergence in at most 3-4 iterations. However, it is found that using the λ_b value from the previous time step improves it by resulting in a convergence in around two steps. The compensation for this additional speed is in the form of memory for storing the λ_b values of the previous time step for each integration direction. The number of orientations considered in this study is very small and hence, λ_b is used as a history variable in our numerical implementation.

4.2. Crystallization Loop

The basic framework of the crystallization loop as implemented in Rastak and Linder (2018) has been adopted for this study. This loop receives the macroscopic crystallinity $\mathbf{\Omega}$, bond stretch λ_b internal variables from the previous time step, in addition to the chain force $\bar{f}$ from the MAPC loop as its input. The crystallinity direction weights χ and the principal stretch directions $\hat{\mathbf{v}}$ are also passed on to this loop. The main functionality of this loop is to update the macroscopic crystallinity variables for the current time step. During this process, it also updates the bond stretch while calculating the current chain stretch vector using the subsumed bond stretch loop.

Initially, the number of contributing principal distribution directions n_{crys} is assumed to be 3. With the help of the crystallinity internal variables, the amount of crystallization ω in each integration direction using (27), along with its gradient and Hessian matrix are calculated. Large values of these gradient and Hessian matrix elements which hinder the convergence of this loop are numerically avoided. The bond stretch loop is then entered to obtain the chain stretch λ and the bond stretch λ_b in each reference orientation. This aids in the calculation of the driving force for crystallization f_w using (15) and then the actual rate of crystallization $\dot{\omega}$ using (16). The rate of evolution of crystallinity variables $\dot{\mathbf{\Omega}}$ is calculated using (31). For an optimized simulation run, the macroscopic distributions along those principal distribution directions, which satisfy $a_i = 0$ and $\dot{a}_i \leq 0$, are neglected as they do not contribute to the calculation of ω in (27). The variable n_{crys} is updated and the loop is started over again with this initial value.

Further, the macroscopic crystallinity internal variables are determined by numerically solving their evolution equation by choosing the residual of the crystallization loop as

$$\boldsymbol{R}_{\Omega} = -\mathbf{\Omega}_{n+1} + \mathbf{\Omega}_n + \Delta t\, \dot{\mathbf{\Omega}}_{n+1}\,. \tag{52}$$

The tangent for this loop can be derived as

$$\boldsymbol{K}_{\Omega} = -\frac{\partial \boldsymbol{R}_{\Omega}}{\partial \mathbf{\Omega}_{n+1}} = \boldsymbol{I}_{4n_{\text{crys}}} - \Delta t \frac{\partial \dot{\mathbf{\Omega}}_{n+1}}{\partial \mathbf{\Omega}_{n+1}}\,. \tag{53}$$

The calculation of this tangent assumes complete convergence of the enclosed bond stretch loop. This makes it reasonable to assume that $R_b = \mathrm{d}R_b = 0$. For simplifying purposes, a modified form of this residual $\tilde{R}_b = -E\lambda_b^2 R_b$ is considered which also satisfies $\tilde{R}_b = \mathrm{d}\tilde{R}_b = 0$ after the convergence of the bond stretch loop. The total change in this residual can be expressed as

$$\mathrm{d}\tilde{R}_b = \frac{\partial \tilde{R}_b}{\partial \lambda}\mathrm{d}\lambda + \frac{\partial \tilde{R}_b}{\partial \lambda_b}\mathrm{d}\lambda_b + \frac{\partial \tilde{R}_b}{\partial \omega}\mathrm{d}\omega = k_{\tilde{R}_b\lambda}\mathrm{d}\lambda + k_{\tilde{R}_b\lambda_b}\mathrm{d}\lambda_b + k_{\tilde{R}_b\omega}\mathrm{d}\omega = 0\,. \tag{54}$$

The above equation can be used to formulate the total change in the bond stretch in terms of the changes in the chain stretch and the degree of crystallization as

$$\mathrm{d}\lambda_b = -\frac{k_{\tilde{R}_b\lambda}}{k_{\tilde{R}_b\lambda_b}}\mathrm{d}\lambda - \frac{k_{\tilde{R}_b\omega}}{k_{\tilde{R}_b\lambda_b}}\mathrm{d}\omega\,. \tag{55}$$

The convergence of the bond stretch loop enables us to write the expression of λ_b in terms of λ and ω, thus reducing the number of independent variables in the problem to two. The chain Jacobian matrix $\boldsymbol{K}$ can be written similar to that in Rastak and Linder (2018) as

$$\boldsymbol{K} = \begin{bmatrix} K_{11} & K_{12} \\ K_{21} & K_{22} \end{bmatrix} = \begin{bmatrix} \left.\dfrac{\partial \bar{f}}{\partial \lambda}\right|_{\tilde{R}_b=0} & \left.\dfrac{\partial \bar{f}}{\partial \omega}\right|_{\tilde{R}_b=0} \\ \left.\dfrac{\partial \dot{\omega}}{\partial \lambda}\right|_{\tilde{R}_b=0} & \left.\dfrac{\partial \dot{\omega}}{\partial \omega}\right|_{\tilde{R}_b=0} \end{bmatrix}. \tag{56}$$

The expressions for each of the Jacobian matrix elements can be derived as explained in Appendix A as

$$
\begin{aligned}
K_{11} &= \frac{1}{k_{\tilde{R}_b\lambda_b}} \frac{\mu}{\lambda_b^2 (1-\omega)\, \mathcal{L}'(\beta)} \left[E\lambda_b (3\lambda_b - 2) - 2\mu \frac{\beta}{\sqrt{N}} \frac{\lambda}{\lambda_b} - \mu\beta^2 (1-\omega) \mathcal{L}'(\beta) \right] \\
K_{12} &= \frac{1}{k_{\tilde{R}_b\lambda_b}} \frac{\mu(\Lambda-1)\sqrt{N}}{\lambda_b (1-\omega)\, \mathcal{L}'(\beta)} \left[E\lambda_b (3\lambda_b - 2) - \mu \frac{\beta}{\sqrt{N}} \frac{\lambda}{\lambda_b} \right] \\
K_{21} &= -\bar{q} K_{12} \\
K_{22} &= \frac{1}{k_{\tilde{R}_b\lambda_b}} \frac{(-\bar{q})}{\mathcal{L}'(\beta)} \left[\frac{\mu N (\Lambda-1)^2}{(1-\omega)} E\lambda_b (3\lambda_b - 2) + \frac{\bar{\xi} k_{\tilde{R}_b\lambda_b}}{(\omega_{\max} - \omega)^2} \right] .
\end{aligned}
\tag{57}
$$

In the above equations, the expression of the quantity $k_{\tilde{R}_b\lambda_b}$ can be written as

$$
k_{\tilde{R}_b\lambda_b} = \frac{\partial \tilde{R}_b}{\partial \lambda_b} = E\lambda_b (3\lambda_b - 2) + \frac{\mu}{(1-\omega)\mathcal{L}'(\beta) N} \left(\frac{\lambda}{\lambda_b} \right)^2 . \tag{58}
$$

With the help of this Jacobian matrix, the gradient of the macroscopic crystallinity rate can be formulated as

$$
\frac{\partial \dot{\boldsymbol{\Omega}}}{\partial \boldsymbol{\Omega}} = \mathcal{A}^{-1} \left(\left\langle \left[\frac{\partial \omega}{\partial \boldsymbol{\Omega}} \right] \left((K_{22} - \frac{K_{12} K_{21}}{K_{11}}) \left[\frac{\partial \omega}{\partial \boldsymbol{\Omega}} \right] - \left[\frac{\partial^2 \omega}{\partial \boldsymbol{\Omega} \partial \boldsymbol{\Omega}} \right] \dot{\boldsymbol{\Omega}} \right)^T \right\rangle + \left\langle \left(\dot{\omega} - \left[\frac{\partial \omega}{\partial \boldsymbol{\Omega}} \right]^T \dot{\boldsymbol{\Omega}} \right) \left[\frac{\partial^2 \omega}{\partial \boldsymbol{\Omega} \partial \boldsymbol{\Omega}} \right] \right\rangle \right) \tag{59}
$$

which is as presented in Rastak and Linder (2018). Inserting (59) into (53), the crystallization loop tangent $\boldsymbol{K}_{\boldsymbol{\Omega}}$ can be calculated.

4.3. MAPC Loop

This is the outermost loop satisfying the MAPC condition while solving for the isochoric first Piola Kirchhoff stress tensor $\bar{\boldsymbol{P}}$ which is the macroscopic counterpart of the chain force. Given the $\bar{\boldsymbol{P}}$, the force vector in each chain with a referential integration direction $\boldsymbol{\lambda}_0$ can be obtained by using (26) as

$$
\bar{\boldsymbol{f}} = 3\bar{\boldsymbol{P}}\boldsymbol{\lambda}_0 . \tag{60}
$$

The magnitude of this force vector is passed on to the bond stretch loop via the crystallization loop as its input. With the given state of deformation represented by $\bar{\boldsymbol{F}}$ and the chain stretch calculated for each integration orientation in the subsumed loops, the MAPC condition is satisfied by considering the MAPC loop residual as

$$
\boldsymbol{R}_\lambda = \frac{1}{3}\bar{\boldsymbol{F}} - \left\langle \lambda \hat{\boldsymbol{\lambda}} \otimes \boldsymbol{\lambda}_0 \right\rangle . \tag{61}
$$

The chain stretch direction $\hat{\boldsymbol{\lambda}}$ is assumed to be in the direction of applied chain force and thus, can be obtained with the help of (60). The calculation of the tangent for this loop assumes that the crystallization loop has completely converged. The derivation of the tangent has been performed in Rastak and Linder (2018) and can be written as

$$
\begin{aligned}
\boldsymbol{K}_\lambda &= -\left(\left. \frac{\partial \boldsymbol{R}_\lambda}{\partial \bar{\boldsymbol{P}}} \right|_{\boldsymbol{\Omega}} + \sum_{i=1}^{4n_{\text{crys}}} \left. \frac{\partial \boldsymbol{R}_\lambda}{\partial \Omega_i} \right|_{\bar{\boldsymbol{P}}} \otimes \left. \frac{\partial \Omega_i}{\partial \bar{\boldsymbol{P}}} \right|_{\boldsymbol{R}_{\boldsymbol{\Omega}}=0} \right) \\
&= 3 \left\langle \left(\frac{\lambda}{\bar{f}} \boldsymbol{I} + \left(\frac{1}{K_{11}} - \frac{\lambda}{\bar{f}} \right) \hat{\boldsymbol{\lambda}} \otimes \hat{\boldsymbol{\lambda}} \right) \bar{\otimes} (\boldsymbol{\lambda}_0 \otimes \boldsymbol{\lambda}_0) \right\rangle \\
&\quad - 3\Delta t \sum_{i=1}^{4n_{\text{crys}}} \left(\left\langle \frac{K_{12}}{K_{11}} \frac{\partial \omega}{\partial \Omega_i} \hat{\boldsymbol{\lambda}} \otimes \boldsymbol{\lambda}_0 \right\rangle \otimes \sum_{j=1}^{4n_{\text{crys}}} \sum_{k=1}^{4n_{\text{crys}}} (K_\Omega)^{-1}_{ij} \mathcal{A}^{-1}_{jk} \left\langle \frac{K_{21}}{K_{11}} \frac{\partial \omega}{\partial \Omega_k} \hat{\boldsymbol{\lambda}} \otimes \boldsymbol{\lambda}_0 \right\rangle \right)
\end{aligned}
\tag{62}
$$

where the tensorial operation $(\boldsymbol{A} \bar{\otimes} \boldsymbol{B})_{abcd} = A_{ac} B_{bd}$.

4.4. Mixed Finite Element Formulation

A three-field mixed finite element formulation developed by Simo and Taylor (1991) has been utilized in conjunction with an augmented Lagrangian multiplier to impose the incompressibility constraint to the problem. Initially, it necessitates the calculation of the isochoric spatial stress and the corresponding tangent modulus. The $\bar{\boldsymbol{P}}$ obtained from the converged MAPC loop is used to find the isochoric spatial stress tensor with the knowledge of its definition given by

$$\bar{\boldsymbol{\tau}} = \bar{\boldsymbol{P}}\bar{\boldsymbol{F}}^T \,. \tag{63}$$

The spatial consistent tangent modulus corresponding to this stress tensor can be formulated assuming Cartesian coordinates as

$$\bar{\mathbb{C}}_{ijkl} = \sum_{A=1}^{3}\sum_{B=1}^{3} \frac{\partial \bar{P}_{iA}}{\partial \bar{F}_{kB}} \bar{F}_{lB}\bar{F}_{jA} - \delta_{ik}\bar{\tau}_{jl} \,. \tag{64}$$

The mixed finite element method utilizes the isochoric spatial stress tensor and its tangent operator obtained from (63) and (64) for calculating the total stress tensor $\boldsymbol{\tau}$ and its corresponding consistent tangent modulus $\mathbb{C}$. Further details about the numerical implementation of this method has been presented in Appendix C.

In the numerical implementation of the whole algorithm, the initial guesses of each loop variable ($\bar{\boldsymbol{P}}$, $\boldsymbol{\Omega}$, $\lambda_{b,l}$) are stored as history variables. For simplifying the formulation, the deformation gradient at the previous time step $\boldsymbol{F}_n$ is also stored, and is utilized along with (18) for obtaining the crystalline direction weights χ and the principal stretch directions $\hat{\boldsymbol{v}}$. For the first time step, the bond stretch in each chain is initialized as $\lambda_b = 1.0$.The macroscopic crystallization variable a is set to zero along all principal distribution directions in order to express the fact that the material has not undergone crystallization yet. The initial value of the spread is taken as $b = 2.0$. On the other hand, for the isochoric first Piola Kirchhoff stress tensor, a linear approximation $\bar{\boldsymbol{P}} \approx \mu\bar{\boldsymbol{F}}$ is used as the initialization value, assuming Gaussian chain model at small strains. At each time step, ϕ_1 and ϕ_2 along each principal distribution direction are initialized to the spherical coordinates of the principal stretch directions $\hat{\boldsymbol{v}}$.

5. Numerical Results

To corroborate the validity of the model presented in the previous sections, experimental data from literature has been used for comparison with their respective numerical simulations. Firstly, the capability of the material model to reproduce the experimental findings of Toki et al. (2003) and of Marchal (Marchal, 2006; Rault et al., 2006) for homogeneous uniaxial loading case without any fracture is studied. In the next study, the ability of the model to capture the behavior of biaxially loaded specimen is studied based on the experimental findings of Chen et al. (2019). Further, the fracture initiation model is validated for non-crystallizing rubber using experimental data for tensile test of double-edge notch specimen from Hocine et al. (2002). Next, the model is validated for crystallizing rubber with different degrees of crystallization from the experimental data for the tensile test of single-edge notch specimen from Gherib et al. (2010). Lastly, a study on the trends of the ultimate fracture stress as compared to the fracture initiation stress predicted by the model is performed for both crystallizing and non-crystallizing rubbers using the experimental data for single-edge notch specimen from Hamed and Park (1999).

As all the fracture initiation studies in this work are mainly uniaxial tensile ones, the point on the surface $\boldsymbol{\Gamma}$ with maximum internal bond stretch energy for rupture was found to be the one ahead of the crack, along its direction and lying on the line of symmetry. This point on the surface of the specimen has been assumed as point P.

5.1. Homogeneous uniaxial tensile tests

The loading and unloading experiments by Toki et al. (2003) for sulfur vulcanized natural rubber (NR-S) is investigated to validate the model for predicting material behavior when subjected to homogeneous uniaxial stress states before fracture initiation. The material parameters used for the simulation are tabulated in Table 1. The uniaxial load is applied at a rate of 0.4 min^{-1}.

It can be observed from Fig. 11 that the fundamental behavior of the strain-induced crystallization process is well captured by the current model. During initial loading, the material exhibits an elastic response as it is devoid of crystals. At higher applied stretches, SIC phenomenon starts, which is indicated by an increase in crystallinity ratio $\bar{\omega}$. However, as SIC is a rate dependent process and is not equilibrated completely during the loading stage, there is a

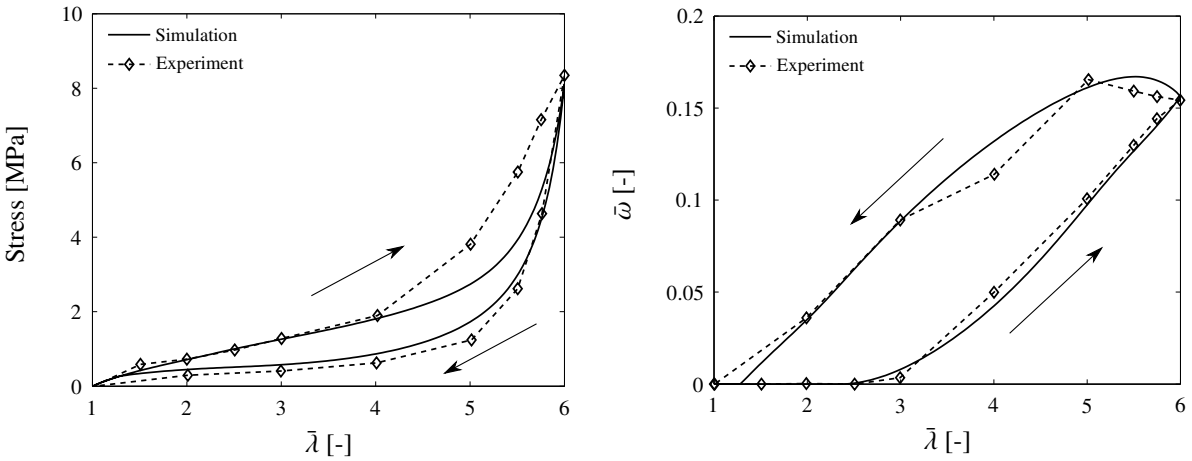

(a) Stress-stretch behavior

(b) Evolution of crystallinity ratio

Figure 11: Homogeneous uniaxial loading case simulation compared with experimental data for sulfur vulcanized natural rubber from Toki et al. (2003).

Table 1: Material parameters used for comparing the homogeneous uniaxial test simulation results with the experimental findings of Toki et al. (2003)

$\mu = nk_BT$	N	$E = nE_b$	α	$\bar{c}$	$\bar{\xi}$	$\omega_{\max}$	$\bar{q}$	p_c
0.37 MPa	18.5	925 MPa	0.37	3.25 MPa	1.0 MPa	0.69	0.015 $\text{MPa}^{-1}\text{min}^{-1}$	1.0

slight observable increase in the crystallinity ratio when unloading starts. With further unloading, crystallinity reduces steadily and finally vanishes. Due to the softening nature of the phenomenon, the stress during unloading is lower than that during loading as the amount of crystallinity is larger during the unloading phase. As per the experimental finding of Marchal (2006), viscous effects are considered negligible and the hysteresis in the stress-stretch response of rubber is assumed to be mainly due to SIC.

Unlike the results predicted by some previous models (Kroon, 2010; Mistry and Govindjee, 2014; Rastak and Linder, 2018), the current model predicts a response that is devoid of a remnant crystallinity upon complete unloading, which is mainly effected by the barrier $\tilde{c}$ function. The more the unloading, the higher is the value of the barrier $\tilde{c}$ as noted in Fig. 5. Physically, this represents an increased tendency of the chains to break out of the crystal due to their relative orientation with respect to the loading direction. Thus, the current model explicitly accounts for the decrease in crystallinity due to an increase in the average angle between the deformed chains $\hat{\boldsymbol{\lambda}}$ and the principal distribution direction $\hat{\boldsymbol{u}}_1$. Hence, it is capable of predicting zero crystallinity upon complete unloading, in line with the experimental findings.

Next, the loading and unloading experiments for different maximum stretches by Marchal (2006) and Rault et al. (2006) is studied. The material parameters used for the simulation are tabulated in Table 2. A homogeneous uniaxial load is applied at a rate of 0.07 min^{-1}.

Table 2: Material parameters used for comparing the homogeneous uniaxial test simulation results with the experimental findings of Rault et al. (2006)

$\mu = nk_BT$	N	$E = nE_b$	α	$\bar{c}$	$\bar{\xi}$	$\omega_{\max}$	$\bar{q}$	p_c
0.22 MPa	23.1	925 MPa	0.33	5.0 MPa	0.05 MPa	0.85	0.015 $\text{MPa}^{-1}\text{min}^{-1}$	1.0

As depicted in Fig. 12, the behavior of the material is captured reasonably well by our model. The major kinks observable in the plots are due to the degree of crystallization ω saturating close to $\omega_{\max}$ in some of the chains during

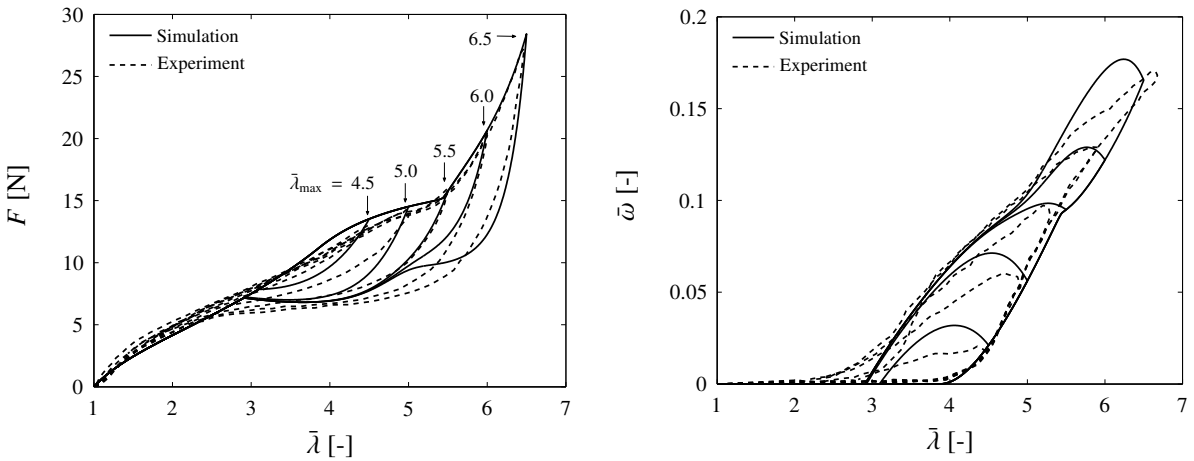

(a) Force-stretch behavior

(b) Evolution of crystallinity ratio

Figure 12: Homogeneous uniaxial loading case simulation for different maximum applied stretch $\bar{\lambda}_{max}$ compared with experimental data from Rault et al. (2006).

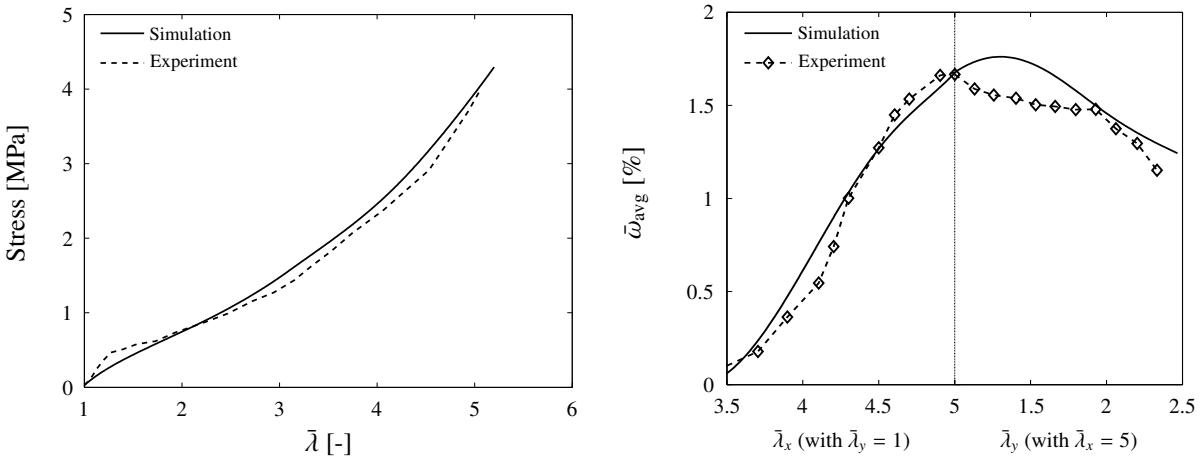

(a) Uniaxial stress-stretch behavior

(b) Sequential biaxial evolution of crystallinity ratio

Figure 13: Prediction of frustration in strain-induced crystallization due to biaxial loading with experimental data from Chen et al. (2019). (a) Uniaxial stress-stretch behavior used for material calibration. (b) Evolution of average crystallinity ratio during sequential biaxial loading.

loading and the delayed start of melting in those chains during unloading.

These two studies clearly demonstrate the capability of our model to predict the material behavior when subjected to homogeneous uniaxial loading.

5.2. Sequential and simultaneous biaxial tensile tests on uniform rectangular specimen

The ability of the model to estimate material behavior when subjected to biaxial loading has been studied using the experimental findings of Chen et al. (2019). The uniaxial behavior of a 75 mm × 75 mm × 0.5 mm film of vulcanized natural rubber as shown in Fig. 13 is primarily used for material calibration. Further, the data of evolution of average value of the crystallinity ratio across all elements $\bar{\omega}_{avg}$ for a sequential biaxial stretching is utilized for fine-tuning the crystallinity parameters. The material parameters used for all simulations in this subsection are tabulated in Table 3.

In the first step of the sequential biaxial loading test, stretch is applied along the X-axis ($\bar{\lambda}_x$) at a rate of $\dot{\varepsilon}_x = 0.8$ min^{-1} until the stretch reaches a value of 5, while keeping the Y-axis displacement fixed ($\bar{\lambda}_y = 1$). In the subsequent

Table 3: Material parameters used for comparing the biaxial test simulation results with the experimental findings of Chen et al. (2019)

$\mu = nk_BT$	N	$E = nE_b$	α	$\bar{c}$	$\bar{\xi}$	$\omega_{\max}$	$\bar{q}$	p_c
0.35 MPa	6.5	7 MPa	0.09	1.8 MPa	0.98 MPa	0.58	0.018 $\text{MPa}^{-1}\text{min}^{-1}$	1.5

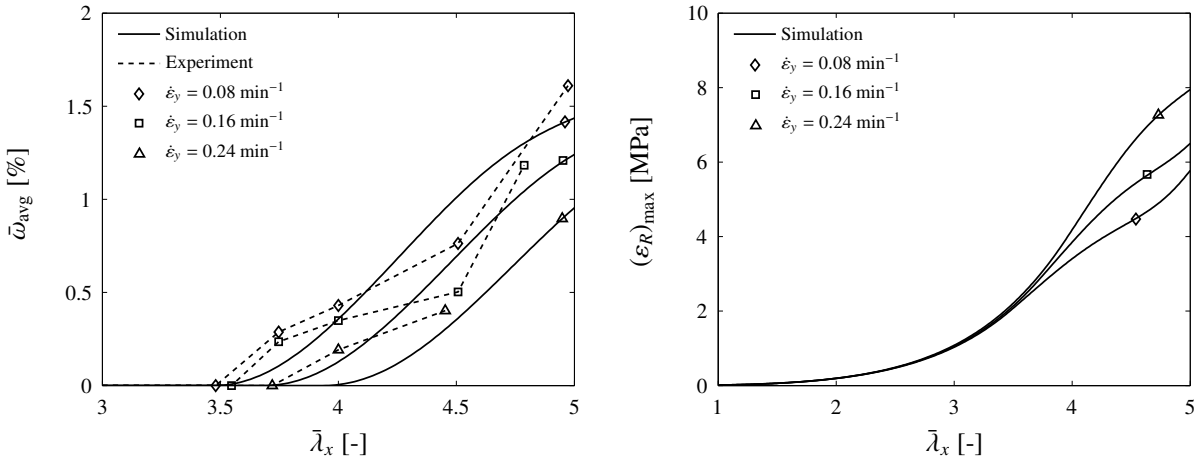

(a) Evolution of crystallinity

(b) Evolution of maximum internal bond energy for rupture

Figure 14: Prediction of behavior when subjected to simultaneous biaxial loading with experimental data from Chen et al. (2019). (a) Comparison of degree of crystallization obtained by simulations with experimental data. (b) Evolution of internal bond energy for rupture as an indicator of the tendency to fracture.

step, $\bar{\lambda}_x$ is kept constant at 5, while $\bar{\lambda}_y$ is applied assuming the same loading rate $\dot{\varepsilon}_y = 0.8$ min^{-1}. It was experimentally observed that the crystallinity ratio decreased with increase in $\bar{\lambda}_y$. The current model is able to capture this frustration in crystallinity due to biaxial loading which is evident from Fig. 13b. When a load in the second direction $\bar{\lambda}_y$ is applied, the average angle between the deformed chains $\hat{\boldsymbol{\lambda}}$ and the initial principal distribution direction $\hat{\boldsymbol{u}}_1$ increases. As a result, some of the chains have a tendency to break out of the crystal. Thus, crystallite melting occurs even though the stretches in the chains do not decrease. This behavior is captured by an increase in the $\tilde{c}$ function in our model. As our model is continuous, a slight increase in crystallinity at a decreasing rate is seen for small values of $\bar{\lambda}_y$.

Using the same material parameters, the behavior of the specimen subjected to simultaneous biaxial loading is studied. In this test, $\bar{\lambda}_x$ is applied at a rate of $\dot{\varepsilon}_x = 0.8$ min^{-1} and simultaneously, $\bar{\lambda}_y$ is also applied at different rates $\dot{\varepsilon}_y$. For processing the experimental data which has been presented in the form of a contour plot in Chen et al. (2019), the rectangular region (3.0,0.5) × (5.1,2.5) of the plot is divided into 99 × 63 grid elements. Using the color bar as reference, the crystallinity ratio value at the center of each element is estimated using its *RGB* value. The value at the required loading points is obtained by first calculating its nearest grid center point and then performing 2D linear interpolation using the values of the 4 nearest neighbors of that point. The plot of the processed experimental data and our simulation results for three different values of $\dot{\varepsilon}_y$ is presented in Fig. 14a. The major trend in evolution of crystallinity ratio is reproduced well by our model. The plot expresses the tendency for delayed initiation of crystallization as lateral stretch $\bar{\lambda}_y$ increases. The current model captures this response by considering an increased barrier $\tilde{c}$ due to an increased competition for crystallite directions. The evolution of the maximum value of internal bond energy for rupture ε_R across all elements has been reported in Fig. 14b. The plot shows an increase in this internal energy value with increasing lateral stretch $\bar{\lambda}_y$. This hints at an increased tendency of specimen subjected to higher $\dot{\varepsilon}_y$ to fracture earlier. This is in line with the experimental findings reported in Chen et al. (2019). As the size of micro-cracks present in the specimen is unknown, our model cannot predict the fracture initiation point.

The potential of the current model to estimate the material behavior when subjected to biaxial loading has been demonstrated by these simulations. The subsequent simulations demonstrate the efficacy of this model to accurately predict the fracture initiation point.

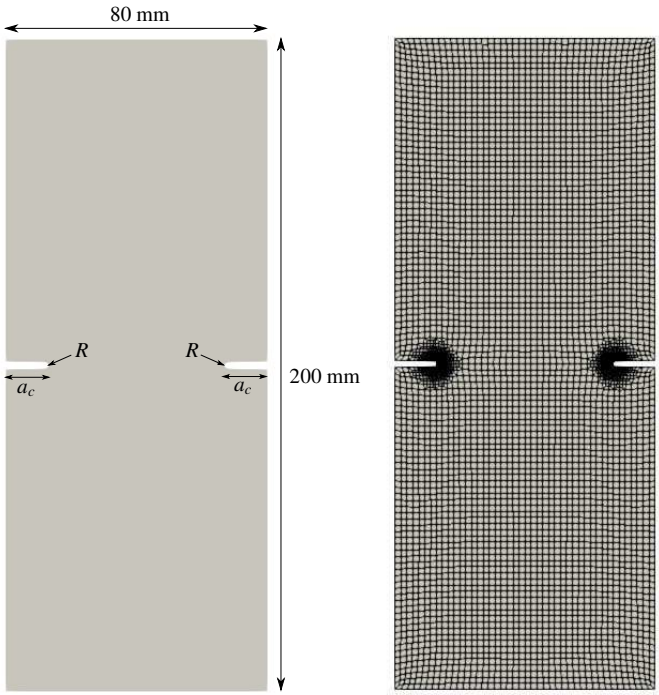

Figure 15: Double-edge notch model with the mesh used for simulations

5.3. Double-edge notch tensile test for non-crystallizing rubber

The fracture initiation in double-edge notched thin sheets of styrene-butadiene rubber (SBR), a non-crystallizing rubber, has been experimentally studied by Hocine et al. (2002). The schematic of the specimen geometry is illustrated in Fig. 15. The dimensions of the specimen are 80 mm × 200 mm × 3 mm. Crack lengths a_c = 12, 16, 20, 24 and 28 mm are considered for the study. For a smoother simulation, cracks are considered to have a very small root radius as a modeling assumption. This radius is usually chosen depending on the dimensions of the specimen for computational tractability. For this simulation, the initial root radius is fixed at R = 1 mm as done in Talamini et al. (2018). The boundary conditions include fixed bottom and top edges with the top-edge being prescribed a vertical strain at a nominal rate of 1×10^{-3} s^{-1}.

Table 4: Material parameters used for comparing the double-edge notch tensile test results with the experimental findings of Hocine et al. (2002)

$\mu = nk_BT$	N	$E = nE_b$	$\varepsilon_{\text{cr}}^f = nN\varepsilon_b^f$	ℓ
0.57 MPa	20	0.12 MPa	0.83 MPa	1 mm

A suitable set of material parameters as shown in Table 4 are used to reproduce the experimental results. Unlike in the work by Talamini et al. (2018) where a large value of N is chosen to model the compressible Neo-Hookean response, a more physically significant value of N is used in this study while considering an incompressible condition. The length scale is appropriately chosen based on the dimensions of the specimen. The value of the critical energy release rate at crack initiation has been estimated using the J-integral in Hocine et al. (2002) and the average value has been reported as $J_c = 1.26\,\text{kJ/m}^2$. A suitable value of the parameter $\varepsilon_{\text{cr}}^f$ has been chosen such that (34) is approximately satisfied.

The ensuing force-displacement curves obtained from simulations are compared with the experimental results in Fig. 16. The plots show the capability of our model to estimate the fracture initiation point with good accuracy. It

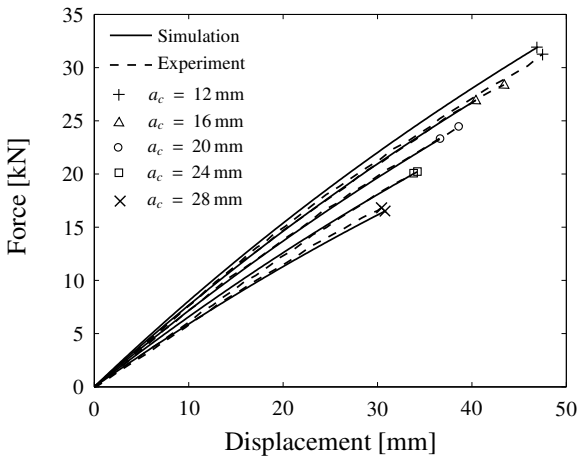

Figure 16: Comparison of fracture initiation points as predicted by the model and experiments by Hocine et al. (2002) for different crack lengths a_c

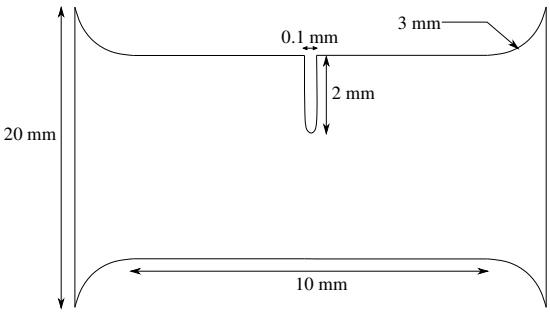

Figure 17: Single edge notch model used for simulations adapted from Gherib et al. (2010). Note that the gripping region of the dumbbell is not considered as it is assumed to be completely fixed due to the grip.

can be observed that with an increase in the crack length, the force required for a particular displacement and the displacement for fracture initiation decreases.

5.4. Single-edge notch tensile test for studying the effect of crystallization on fracture initiation

The fracture initiation and rupture properties of SBR and NR were experimentally studied by Gherib et al. (2010). In the NR sample, the effect of crystallization on these properties is studied by subjecting the notched specimen to tensile stretch at different strain rates.

Table 5: Calibrated material parameters using the unnotched specimen behavior reported in Gherib et al. (2010) for non-crystallizing SBR

$\mu = nk_BT$	N	$E = nE_b$	$\varepsilon_{\text{cr}}^f = nN\varepsilon_b^f$	ℓ
0.3 MPa	17	0.95 MPa	11.0 MPa	0.1 mm

The stress-stretch behavior of unnotched samples of both SBR and NR, depicted by Fig. 18a and Fig. 19a, were mainly used for calibration of material parameters (except $\varepsilon_{\text{cr}}^f$ and ℓ) as shown in Table 5 and Table 6. In crystallizing rubber, the curve for the higher strain rate of $\dot{\varepsilon} = 25\ \text{min}^{-1}$ was used as the primary source for calibration purposes. The experimental curve for the unnotched NR specimen at the lower strain rate of $\dot{\varepsilon} = 1\ \text{min}^{-1}$ showed a rupture stretch of $\bar{\lambda}_{\text{rup}} = 6.5$ while that of the notched specimen at the same strain rate is reported to be $\bar{\lambda}_{\text{rup}} = 10.3$, which is an anomaly. Also, a slower strain rate is expected to provide more time for crystallization to occur, which would result in a softer response. Hence, the experimental curve for the slower strain rate was not chosen.

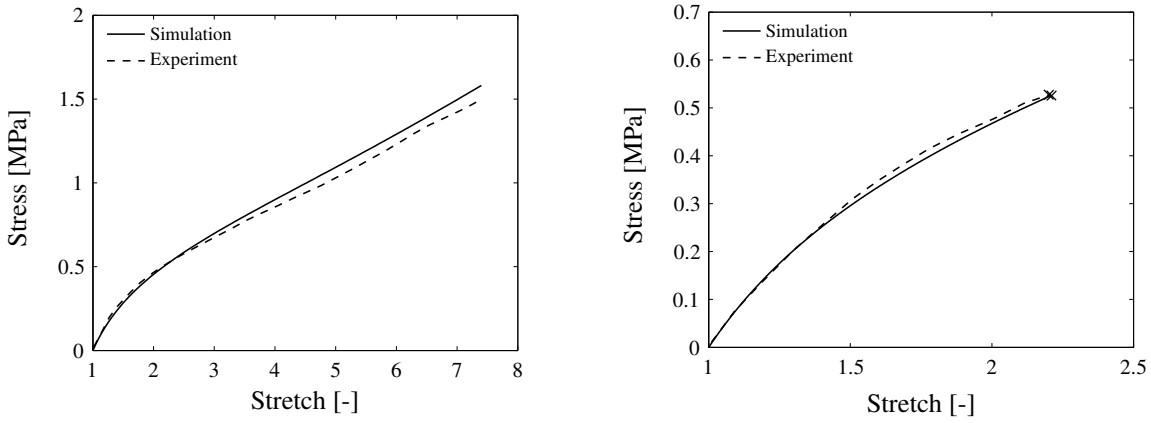

(a) Unnotched specimen behavior

(b) Notched specimen behavior

Figure 18: Prediction of fracture initiation in non-crystallizing SBR. (a) Uniaxial tensile behavior of unnotched sample used for material calibration. (b) Stress-stretch behavior up to fracture initiation in single edge notched specimen predicted using calibrated material model compared with experimental data from Gherib et al. (2010). Cross marks indicate the point of crack initiation.

Neglecting the gripping portion of the dumbbell which was assumed to be completely fixed, the single-edge notch specimen with an out-of-plane thickness of 2 mm used for the simulation is as shown in Fig. 17. The same material parameters calibrated using the unnotched samples are used. An appropriate length scale has been chosen depending on the dimensions of the problem. The values of the critical energy release rate measured using the J-integral has been quoted to be in the range of 3.0-3.4 kJ/m^2 for SBR and 12.2-23.7 kJ/m^2 for NR at the point of crack initiation. The values of $\varepsilon^f_{\text{cr}}$ were chosen keeping in mind to approximately satisfy (34). The approximations made in the case for crystallizing rubbers for (34) to hold, as explained in Remark 4, can be utilized to justify the relatively smaller value of $\varepsilon^f_{\text{cr}}$ used for them.

Table 6: Calibrated material parameters using the unnotched specimen behavior reported in Gherib et al. (2010) for crystallizing NR

μ	N	E	α	$\bar{c}$	$\bar{\xi}$	$\omega_{\max}$	$\bar{q}$	p_c	$\varepsilon^f_{\text{cr}}$	ℓ
0.35 MPa	20	5.2 MPa	0.37	1.0 MPa	0.98 MPa	0.5	0.018 MPa^{-1}min^{-1}	2.0	23.8 MPa	0.1 mm

With the help of the chosen material parameters, the simulated stretch-stress response for the notched samples of both SBR and NR are compared with the experimental curves. In addition to the previous result in Section 5.3, the good agreement of results as shown in Fig. 18b corroborates the effectiveness of our model in predicting the fracture initiation point in non-crystallizing rubbers like SBR. In the study of crystallizing NR, the case with $\dot{\varepsilon} = 1\,\text{min}^{-1}$ had a delayed crack initiation as the slower strain rate is more conducive for the crystallization process as seen in Fig. 19c. As observed in Fig. 19b, the model captures the phenomenon of delayed fracture initiation with higher crystallization with great precision.

For a better comprehension, a study of the evolution of the internal bond stretch energy for rupture ε_R for both the strain rate cases has been presented. Fig. 19d represents the variation of this value at the point of consideration, $X = P$. The contour plots of ε_R in the whole domain of the model as shown in Fig. 20, also show a similar distribution in the early stages of the stretching process. As the stretch increases, crystallization inhibits the increase in ε_R for the case of $\dot{\varepsilon} = 1\,\text{min}^{-1}$ and hence, a smaller spread is observed as compared to the case of $\dot{\varepsilon} = 25\,\text{min}^{-1}$. In this way, the delayed fracture initiation is captured and hence, it can be concluded that the model qualitatively and quantitatively predicts the effect of crystallization on the crack initiation point efficiently.

5.5. Single-edge notch tensile test for comparison with ultimate fracture stress

The study on the general trend between the fracture initiation and ultimate fracture stresses for notched samples of both SBR and NR has been presented here. The experimental study on the rupture of vulcanizates of SBR and NR

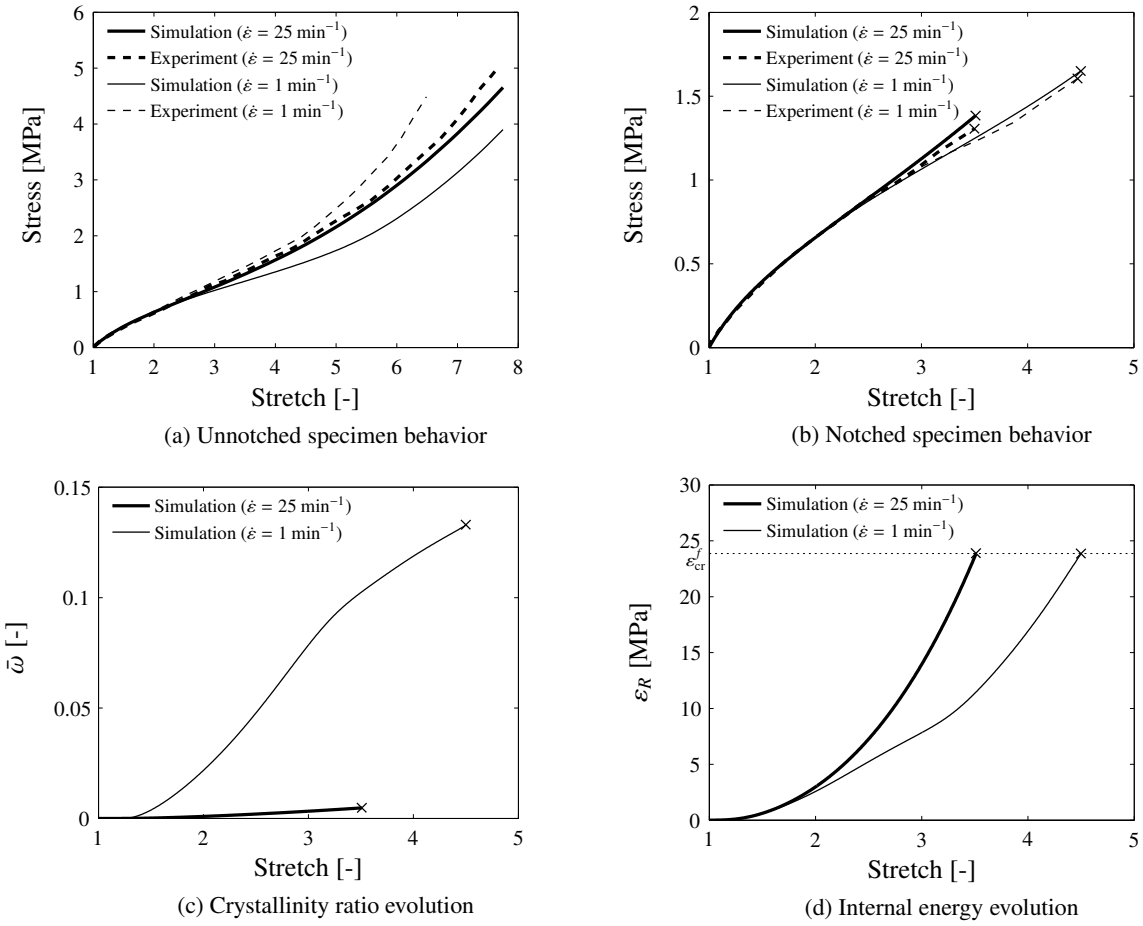

(a) Unnotched specimen behavior

(b) Notched specimen behavior

(c) Crystallinity ratio evolution

(d) Internal energy evolution

Figure 19: Prediction of fracture initiation in crystallizing NR. (a) Uniaxial tensile behavior of unnotched sample for two strain rates. Material calibrated using the experimental curve for $\dot{\varepsilon} = 25$ min^{-1} and simulation curve for the case of $\dot{\varepsilon} = 1$ min^{-1} is produced using the above calibrated parameters as its experimental curve is found to be an anomaly. (b) Stress-stretch behavior up to fracture initiation in single edge notched specimen predicted using calibrated material model compared with experimental data from Gherib et al. (2010). (c) Evolution of crystallinity ratio $\bar{\omega}$ and (d) Evolution of the internal bond energy for rupture ε_R at point $X = P$. Cross marks indicate the point of crack initiation.

performed by Hamed and Park (1999) has been used for the purpose of calibrating the model and for the comparison study.

Table 7: Calibrated material parameters using the unnotched specimen behavior used for comparison with the experimental findings of Hamed and Park (1999)

Type	μ	N	E	α	$\bar{c}$	$\bar{\xi}$	$\omega_{\max}$	$\bar{q}$	p_c	ε^f_{cr}	ℓ
SBR	0.58 MPa	10	6.5 MPa	-	-	-	-	-	-	0.75 MPa	0.1 mm
NR	0.49 MPa	8	9.5 MPa	0.37	0.35 MPa	0.98 MPa	0.5	0.018 MPa^{-1}min^{-1}	2.0	2.4 MPa	0.1 mm

The stretch-stress behavior of the unnotched samples as shown in Fig. 21a have been used for calibration of the material parameters (except ε^f_{cr} and ℓ) presented in Table 7. For the NR sample, approximately the first 70% of the behavior presented in their work is only considered. The reason is that the restraining effect of crystallization to the propagation of the micro-cracks that form before the rupture of the unnotched specimens is not considered in the proposed model. The empirical 70% is used as it was found that similar parameters can be used for modeling the

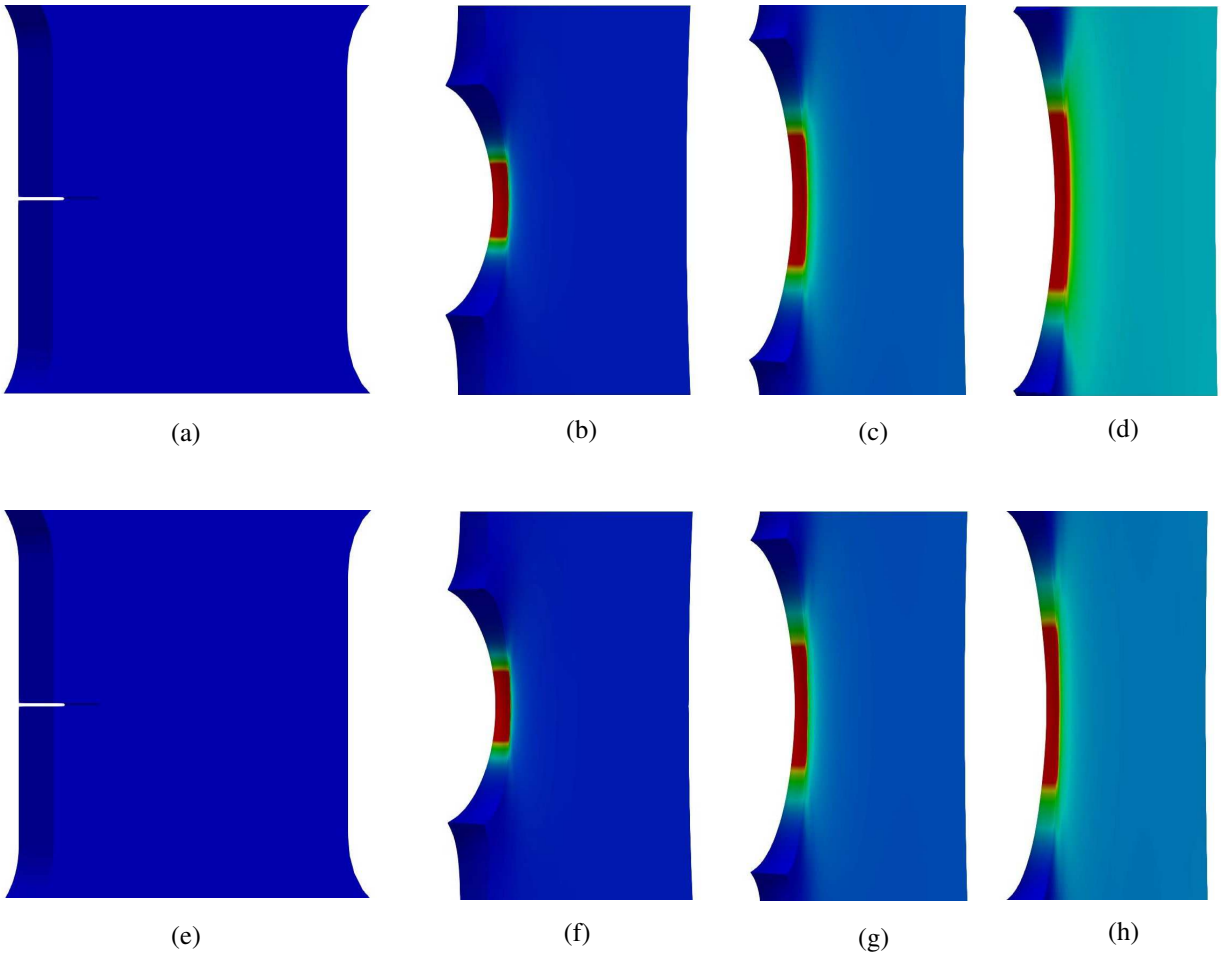

Figure 20: Evolution of internal bond stretch energy for rupture ε_R in notched sample of crystallizing NR material. Figures (a)-(d) represent the distribution for the case of $\dot{\varepsilon} = 25\ \text{min}^{-1}$ for applied stretches of 1, 2.25, 3, 3.51 (fracture initiation stretch), respectively. Figures (e)-(h) represent the respective counterparts for the mentioned applied stretches for the case of $\dot{\varepsilon} = 1\ \text{min}^{-1}$. To aid visualization, custom range of color scheme has been set to [0 MPa, 5 MPa].

behavior below this value, as the slope of the curve is nearly the same. It is also an approximation of the ratio of crack initiation stretch to the rupture stretch from the experimental study by Gherib et al. (2010).

Single edge notched strip specimens of dimensions 12.5 mm × 60 mm × 2 mm (with the height of 60 mm equal to the experimental initial separation between clamps) were used for the simulations. Varying crack widths with the crack root radius as $R = 0.1$ mm were modeled for the study. The length scale ℓ was chosen considering the dimensions of the problem and a corresponding critical internal energy $\varepsilon_{\text{cr}}^{f}$ was approximated to satisfy (34). However, as the tearing energy presented by Hamed and Park (1999) is calculated at the point of complete fracture, conservative approximations of $\varepsilon_{\text{cr}}^{f}$ were made based on these estimates.

The trend of the fracture initiation stress predicted from simulation is compared with that of the experimental ultimate fracture stress as shown in Fig. 21b. The simulation results for SBR show a good agreement with the trend of the experimental ultimate fracture stress. As the crack lengths increase, the difference between the crack initiation and ultimate fracture stresses reduces mainly because of the smaller distance for the crack to propagate. For smaller crack lengths of NR, bulk crystallization and its resistance to the crack growth is attributed to the high ultimate fracture stresses as explained in Thomas and Whittle (1970) and Rong et al. (2016). Since the model does not account for that, the trend is not captured. However, the simulated trend is in reasonable agreement with that of the experimental results for larger cracks wherein the effect of crystallization on the crack propagation is smaller. This result not only reflects

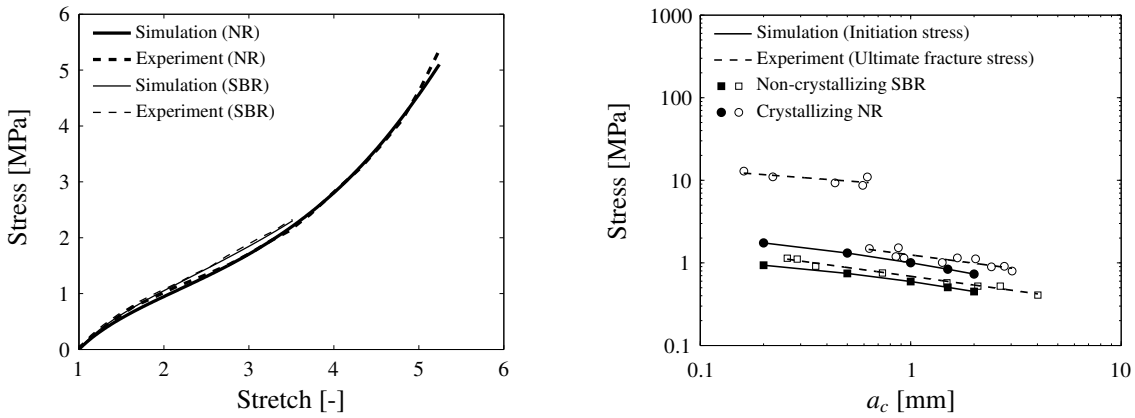

(a) Unnotched specimen behavior

(b) Notched specimen behavior

Figure 21: Comparison of the predicted failure initiation stress with experimental ultimate fracture stress of both SBR and NR. (a) Uniaxial tensile behavior of unnotched samples used for material calibrations; Only the initial 70% of the total experimental stretch behavior is considered here for crystallizing NR. (b) Predicted trends for specimen of different crack lengths a_c compared with the experimental data from Hamed and Park (1999)

.

the ability of our model to capture the trend in fracture initiation points in both crystallizing and non-crystallizing rubbers, but also demonstrates the utility of the model in roughly estimating the ultimate fracture stresses for most cases without the need for modeling the crack propagation.

6. Conclusion

A micromechanical energy based fracture criterion has been proposed in this study for predicting the fracture initiation in rubber-like polymers with pre-existing cracks, by taking into account the effect of strain-induced crystallization. A multi-scale formulation of the material has been developed for characterizing the polymer behavior when subjected to both uniaxial and biaxial loading. At the microscale, the chain segments, including the crystallized ones, have been modeled as elastic to account for the internal energy due to atomistic bond distortions, the main contributor to the critical energy for crack initiation. In the chain formulation, the effects of the loading condition and the relative orientation of chains with respect to the principal stretching directions on the incremental interface energy of crystalline phase have been taken into account. A homogenization model called Maximal Advance Path Constraint has been utilized for bridging this microscale model with the macroscale formulation which uses an existing crystallinity distribution function. The ability of this network model to account for anisotropy in stretched states makes it a perfect choice for fracture modeling applications. The rigidity of the crystallites has been taken into account by introducing a crystallite distortion energy as a part of the critical energy for rupture. This model has been validated by comparison with existing experimental results. The material behavior during homogeneous uniaxial tensile tests has been well estimated by the model. The model also has demonstrated the capability of predicting a frustration in crystallization with biaxial loading. The crack initiation points for both crystallizing and non-crystallizing rubbers have been predicted with good accuracy by the model. The model could also qualitatively and quantitatively forecast the effect of crystallization with good precision. The trends for ultimate fracture stresses for different crack lengths in both types of rubbers have been estimated well by the model.

This study on the fracture initiation prediction has been envisioned as a stepping stone towards modeling the fracture in crystallizing rubbers. In this regard, our model can be improved by incorporating the fracture model for elastomers using phase-field approach by Talamini et al. (2018) for simulating the crack propagation through crystallizing rubbers and for accurately predicting the ultimate fracture stresses. With more experimental data, the model can be improved to estimate the crystallite directions during biaxial loading. Similarly, with more experimental studies, the efficacy of the model in predicting fracture initiation in biaxially loaded specimen should also be verified.

Acknowledgements

Financial support for this research was provided by the National Science Foundation through CAREER Award CMMI-1553638 and the Department of Energy, National Nuclear Security Administration under Award Number DE-NA0003962. This support is gratefully acknowledged.

Appendix A. Derivation of chain quantities

A derivation following the steps done in Rastak and Linder (2018) is shown here for the case of partially crystallized chain with degree of crystallization ω. The case $\omega \to 0$ and $\mathrm{d}\omega \to 0$ converges to the case of non-crystallizing rubbers. Based on Fig. 1 and Fig. 3, the relative stretch Langevin parameter can be derived starting from (10) as

$$\Lambda = \frac{r_a}{L_a} = \frac{r - L_c}{L - L_c} = \frac{\lambda r_0 - N_c l}{N l - N_c l} = \frac{\lambda\left(\sqrt{N} l_0\right) - (N\omega)\,(\lambda_b l_0)}{N\,(\lambda_b l_0) - (N\omega)\,(\lambda_b l_0)} = \frac{\lambda/(\lambda_b\sqrt{N}) - \omega}{1 - \omega}\,. \tag{A.1}$$

Using this, the amorphous part of the free energy can be calculated starting from (3) as

$$\psi_a\,(\lambda, \lambda_b, \omega) = \int_0^r F\left(r^\star\right)\mathrm{d}r^\star = \int_0^\lambda \frac{k_B T \beta\,(\lambda^\star)}{l}\left(\sqrt{N} l_0\,\mathrm{d}\lambda^\star\right)\,. \tag{A.2}$$

For a given value of λ_b and ω, the relationship between the change in λ and Λ can be derived from (10) as

$$\mathrm{d}\lambda = \sqrt{N}\lambda_b\,(1 - \omega)\,\mathrm{d}\Lambda\,. \tag{A.3}$$

Assuming that the relative stretch of the segment Λ is non-negative by imposing an initial $\Lambda = 0$ condition, the integral in (A.2) is simplified using integration by parts as

$$\psi_a\,(\lambda, \lambda_b, \omega) = \int_0^\Lambda \frac{k_B T \beta\,(\Lambda^\star)\,\sqrt{N}}{\lambda_b}\left(\sqrt{N}\lambda_b\,(1 - \omega)\;\mathrm{d}\Lambda^\star\right) = k_B T N\,(1 - \omega)\left(\Lambda\beta - \int_0^\beta \Lambda\left(\beta^\star\right)\mathrm{d}\beta^\star\right)\,. \tag{A.4}$$

Using the Langevin function, the integral of Λ can be expressed as

$$-\int_0^\beta \Lambda\left(\beta^\star\right)\mathrm{d}\beta^\star = -\int_0^\beta \left(\coth\beta^\star - \frac{1}{\beta^\star}\right)\mathrm{d}\beta^\star = -\left(\ln\left(\sinh\beta\right) - \ln\beta\right) = \ln\frac{\beta}{\sinh\beta}\,. \tag{A.5}$$

Substituting (A.5) in (A.4), the expression for the free energy in crystallizing chains is obtained as in (11). Similarly, for the case of non-crystallizing rubbers ($\omega \to 0$), the expression for $\psi_a\,(\lambda, \lambda_b)$ can be written as

$$\psi_a\,(\lambda, \lambda_b) = k_B T N\left(\Lambda\beta + \ln\frac{\beta}{\sinh\beta}\right) \quad \text{with} \quad \Lambda = \frac{\lambda}{(\lambda_b\sqrt{N})}\,. \tag{A.6}$$

It can be observed that the expression for ψ_a looks similar to (3) while the effect of bond stretch is incorporated by the Langevin parameters. For obtaining the free energy density, it can be normalized with the number of chains per unit referential volume as done in (19).

The bond stretch is calculated as the minimizer of the free energy density. The implicit equation can be derived by minimizing the normalized free energy as

$$\begin{aligned}
\frac{\partial\bar{\psi}}{\partial\lambda_b} &= N\frac{\mathrm{d}\varepsilon_b}{\mathrm{d}\lambda_b} + \mu N\,(1 - \omega)\,\frac{\partial}{\partial\lambda_b}\left(\beta\Lambda + \ln\frac{\beta}{\sinh\beta}\right) + \frac{\partial}{\partial\lambda_b}\psi_c\,(\omega) = 0 \\
&= NE\,(\lambda_b - 1) + \mu N\,(1 - \omega)\beta\frac{\partial\Lambda}{\partial\lambda_b} = 0 \\
&= NE\,(\lambda_b - 1) - \mu N\,(1 - \omega)\beta\frac{\lambda}{\lambda_b^2\sqrt{N}\,(1 - \omega)} = 0\,.
\end{aligned} \tag{A.7}$$

This equation can be solved using Newton's method iteratively. It is well known that the floating point precision of computers is 10^{-16}, which is the minimum error introduced by even addition or subtraction of real numbers. Hence, the expression of the residual was chosen as shown in (46) in order to optimally minimize the numerical errors. For all practical purposes, as the magnitude of λ_b roughly lies in the range [1,10], the chosen residual can be satisfied up to a precision of 10^{-15} error which is of primary importance as the bond stretch loop forms the innermost loop among three Newton loops and the errors are carried forward.

For the calculation of the tangent for the bond stretch loop, let us evaluate each of the terms in (47). Taking the partial derivative of the residual with respect to λ_b and λ, we get

$$\frac{\partial R_b}{\partial \lambda_b} = -1 + \frac{\mu}{E\sqrt{N}}\left(-2\beta\frac{\lambda}{\lambda_b^3} + \frac{\lambda}{\lambda_b^2}\frac{1}{\mathcal{L}'(\beta)}\left(-\frac{\lambda}{\lambda_b^2\sqrt{N}}\frac{1}{1-\omega}\right)\right) \tag{A.8}$$

$$\frac{\partial R_b}{\partial \lambda} = \frac{\mu}{E\sqrt{N}}\left(\beta\frac{1}{\lambda_b^2} + \frac{\lambda}{\lambda_b^2}\frac{1}{\mathcal{L}'(\beta)}\left(\frac{1}{\lambda_b\sqrt{N}}\frac{1}{1-\omega}\right)\right). \tag{A.9}$$

Using (A.8), (A.9) and (49), the expression for the bond stretch loop tangent can be obtained as shown in (51). For obtaining (50), the expression for the change in the chain force is considered. Starting from the expression for the chain force due to the stretch as obtained in (14) and using normalizations given by (19) and (20), we can write

$$\begin{aligned}
\mathrm{d}\bar{f} &= \mathrm{d}\left(\mu\sqrt{N}\frac{\beta}{\lambda_b}\right)\\
&= \mu\sqrt{N}\frac{1}{\lambda_b}\left(\frac{1}{\mathcal{L}'(\beta)}\mathrm{d}\Lambda - \frac{\beta}{\lambda_b}\mathrm{d}\lambda_b\right)\\
&= \mu\sqrt{N}\frac{1}{\lambda_b}\left(\frac{1}{\mathcal{L}'(\beta)}\left(\frac{1}{\lambda_b\sqrt{N}}\mathrm{d}\lambda - \frac{\lambda}{\lambda_b^2\sqrt{N}}\mathrm{d}\lambda_b + (\Lambda-1)\,\mathrm{d}\omega\right)\frac{1}{1-\omega} - \frac{\beta}{\lambda_b}\mathrm{d}\lambda_b\right)\\
&= \frac{\mu}{\lambda_b^2(1-\omega)\mathcal{L}'(\beta)}\mathrm{d}\lambda - \left(\frac{\mu\lambda}{\lambda_b^3(1-\omega)\mathcal{L}'(\beta)} + \frac{\mu\beta\sqrt{N}}{\lambda_b^2}\right)\mathrm{d}\lambda_b + \frac{\mu\sqrt{N}(\Lambda-1)}{\lambda_b(1-\omega)\mathcal{L}'(\beta)}\mathrm{d}\omega\\
&= k_{\bar{f}\lambda}\mathrm{d}\lambda + k_{\bar{f}\lambda_b}\mathrm{d}\lambda_b + k_{\bar{f}\omega}\mathrm{d}\omega\,.
\end{aligned} \tag{A.10}$$

The calculation of the Jacobian matrix $\boldsymbol{K}$ in (56) requires the consideration of the amount of change in $\dot{\omega}$.

$$\begin{aligned}
\mathrm{d}\dot{\omega} &= \mathrm{d}\left(\bar{q}\bar{f}_w\right)\\
&= \bar{q}\,\mathrm{d}\left(\mu N\left(\beta + \ln\frac{\beta}{\sinh\beta}\right) - \tilde{c} - \frac{\bar{\xi}\omega}{\omega_{\max}(\omega_{\max}-\omega)}\right)\\
&= \bar{q}\mu N(\mathrm{d}\beta - \Lambda\mathrm{d}\beta) - \bar{q}\frac{\bar{\xi}\mathrm{d}\omega}{(\omega_{\max}-\omega)^2}\\
&= \bar{q}\mu N\frac{(1-\Lambda)}{(1-\omega)\mathcal{L}'(\beta)}\left(\frac{1}{\lambda_b\sqrt{N}}\mathrm{d}\lambda - \frac{\lambda}{\lambda_b^2\sqrt{N}}\mathrm{d}\lambda_b + (\Lambda-1)\,\mathrm{d}\omega\right) - \bar{q}\frac{\bar{\xi}\mathrm{d}\omega}{(\omega_{\max}-\omega)^2}\\
&= \frac{\bar{q}\mu\sqrt{N}(1-\Lambda)}{\lambda_b(1-\omega)\mathcal{L}'(\beta)}\mathrm{d}\lambda - \frac{\bar{q}\mu\sqrt{N}(1-\Lambda)\lambda}{\lambda_b^2(1-\omega)\mathcal{L}'(\beta)}\mathrm{d}\lambda_b - \left(\frac{\bar{q}\mu N(\Lambda-1)^2}{(1-\omega)\mathcal{L}'(\beta)} + \frac{\bar{q}\bar{\xi}}{(\omega_{\max}-\omega)^2}\right)\mathrm{d}\omega\\
&= k_{\dot{\omega}\lambda}\mathrm{d}\lambda + k_{\dot{\omega}\lambda_b}\mathrm{d}\lambda_b + k_{\dot{\omega}\omega}\mathrm{d}\omega
\end{aligned} \tag{A.11}$$

The crystallization loop assumes that the bond stretch loop has converged completely so that the changes in λ_b

can be expressed in terms of λ and ω itself as shown in (55). Using (54), we get

$$\begin{aligned}
\mathrm{d}\tilde{R}_b &= \mathrm{d}\left(E\lambda_b^2\left(\lambda_b-1\right)-\mu\beta\frac{\lambda}{\sqrt{N}}\right)\\
&= E\lambda_b\left(3\lambda_b-2\right)\mathrm{d}\lambda_b-\mu\beta\frac{\mathrm{d}\lambda}{\sqrt{N}}-\mu\frac{\lambda}{\sqrt{N}}\mathrm{d}\beta\\
&= E\lambda_b\left(3\lambda_b-2\right)\mathrm{d}\lambda_b-\mu\beta\frac{\mathrm{d}\lambda}{\sqrt{N}}-\mu\frac{\lambda}{\sqrt{N}\left(1-\omega\right)\mathcal{L}'\left(\beta\right)}\left(\frac{1}{\lambda_b\sqrt{N}}\mathrm{d}\lambda-\frac{\lambda}{\lambda_b^2\sqrt{N}}\mathrm{d}\lambda_b+\left(\Lambda-1\right)\mathrm{d}\omega\right)\\
&= \left(-\frac{\mu\beta}{\sqrt{N}}-\frac{\mu\lambda}{\lambda_b N\left(1-\omega\right)\mathcal{L}'\left(\beta\right)}\right)\mathrm{d}\lambda+\left(E\lambda_b\left(3\lambda_b-2\right)+\frac{\mu\lambda^2}{\lambda_b^2 N\left(1-\omega\right)\mathcal{L}'\left(\beta\right)}\right)\mathrm{d}\lambda_b\\
&\qquad -\frac{\mu\lambda\left(\Lambda-1\right)}{\sqrt{N}\left(1-\omega\right)\mathcal{L}'\left(\beta\right)}\mathrm{d}\omega\\
&= k_{\tilde{R}_b\lambda}\mathrm{d}\lambda+k_{\tilde{R}_b\lambda_b}\mathrm{d}\lambda_b+k_{\tilde{R}_b\omega}\mathrm{d}\omega\,.
\end{aligned}\tag{A.12}$$

From the above derivations and using (55), equations (A.10) and (A.11) can be rephrased as

$$\begin{aligned}
\mathrm{d}\bar{f} &= k_{\bar{f}\lambda}\mathrm{d}\lambda+k_{\bar{f}\lambda_b}\mathrm{d}\lambda_b+k_{\bar{f}\omega}\mathrm{d}\omega\\
&= k_{\bar{f}\lambda}\mathrm{d}\lambda+k_{\bar{f}\lambda_b}\left(-\frac{k_{\tilde{R}_b\lambda}}{k_{\tilde{R}_b\lambda_b}}\mathrm{d}\lambda-\frac{k_{\tilde{R}_b\omega}}{k_{\tilde{R}_b\lambda_b}}\mathrm{d}\omega\right)+k_{\bar{f}\omega}\mathrm{d}\omega\\
&= \left(k_{\bar{f}\lambda}-k_{\bar{f}\lambda_b}\frac{k_{\tilde{R}_b\lambda}}{k_{\tilde{R}_b\lambda_b}}\right)\mathrm{d}\lambda+\left(k_{\bar{f}\omega}-k_{\bar{f}\lambda_b}\frac{k_{\tilde{R}_b\omega}}{k_{\tilde{R}_b\lambda_b}}\right)\mathrm{d}\omega\\
&= K_{11}\mathrm{d}\lambda+K_{12}\mathrm{d}\omega
\end{aligned}\tag{A.13}$$

$$\begin{aligned}
\mathrm{d}\dot{\omega} &= k_{\dot{\omega}\lambda}\mathrm{d}\lambda+k_{\dot{\omega}\lambda_b}\mathrm{d}\lambda_b+k_{\dot{\omega}\omega}\mathrm{d}\omega\\
&= k_{\dot{\omega}\lambda}\mathrm{d}\lambda+k_{\dot{\omega}\lambda_b}\left(-\frac{k_{\tilde{R}_b\lambda}}{k_{\tilde{R}_b\lambda_b}}\mathrm{d}\lambda-\frac{k_{\tilde{R}_b\omega}}{k_{\tilde{R}_b\lambda_b}}\mathrm{d}\omega\right)+k_{\dot{\omega}\omega}\mathrm{d}\omega\\
&= \left(k_{\dot{\omega}\lambda}-k_{\dot{\omega}\lambda_b}\frac{k_{\tilde{R}_b\lambda}}{k_{\tilde{R}_b\lambda_b}}\right)\mathrm{d}\lambda+\left(k_{\dot{\omega}\omega}-k_{\dot{\omega}\lambda_b}\frac{k_{\tilde{R}_b\omega}}{k_{\tilde{R}_b\lambda_b}}\right)\mathrm{d}\omega\\
&= K_{21}\mathrm{d}\lambda+K_{22}\mathrm{d}\omega\,.
\end{aligned}\tag{A.14}$$

Putting in the values from the previous derivations, the elements of the Jacobian matrix $\boldsymbol{K}$ can be obtained as presented in (57). Further calculations for the crystallization and MAPC loops are implemented in a similar fashion as done in Rastak and Linder (2018) and this study can be referred for detailed derivations.

Appendix B. Visualization of crystallinity distribution

The efficacy of the macroscopic crystallinity model obtained by a simple linear combination of distributions assumed along the three principal distribution directions given by (27) is studied in this section. The loading conditions assumed are: (1) $\boldsymbol{F}_{\text{uniaxial}}=\bar{\lambda}\,\boldsymbol{e}_1\otimes\boldsymbol{e}_1+\bar{\lambda}^{-1/2}\,\boldsymbol{e}_2\otimes\boldsymbol{e}_2+\bar{\lambda}^{-1/2}\,\boldsymbol{e}_3\otimes\boldsymbol{e}_3$; (2) $\boldsymbol{F}_{\text{equibiaxial}}=\bar{\lambda}\,\boldsymbol{e}_1\otimes\boldsymbol{e}_1+\bar{\lambda}\,\boldsymbol{e}_2\otimes\boldsymbol{e}_2+\bar{\lambda}^{-2}\,\boldsymbol{e}_3\otimes\boldsymbol{e}_3$. The parameters used for the simulation are tabulated in Table B.8.

Table B.8: Parameters used for the visualization of the macroscopic crystallinity distribution

μ	N	$E=nE_b$	$\bar{c}$	$\bar{\xi}$	$\omega_{\max}$	$\bar{q}$	p_c	$\dot{\varepsilon}$
0.37 MPa	18.5	925 MPa	1.2 MPa	1.0 MPa	0.69	0.015 $\text{MPa}^{-1}\text{min}^{-1}$	2.0	0.4 min^{-1}

The crystallinity distribution is visualized for different applied principal stretches $\bar{\lambda}$ for both the loading cases. For the uniaxial tensile case, at smaller stretch, Fig. B.22a depicts crystallization in chains only along a few orientations

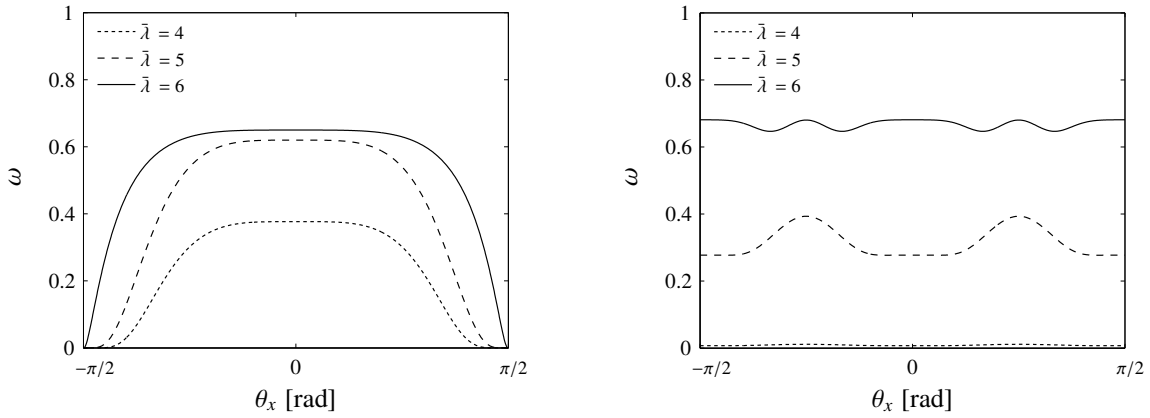

(a) Uniaxial Tension (b) Equibiaxial Tension

Figure B.22: Visualization of the crystallinity distribution of chains in XY plane making an angle θ_x with the X-axis. (a) Uniaxial and (b) Equibiaxial loading cases are considered for different applied principal stretches $\bar{\lambda}$.

around the principal stretch direction. This spread increases with the applied stretch, while the maximum magnitude saturates due to the effects of entanglements. For the equibiaxial tensile case, Fig. B.22b depicts a delayed initiation of crystallization. At higher stretches, even though not perfect, the model reasonably predicts an isotropic evolution of the crystallinity distribution. As compared to the model in our previous study (Rastak and Linder, 2018) wherein macroscopic crystallinity distribution is assumed along one principal crystallite direction, the current model is capable of capturing the crystallinity along different directions caused due to multiaxial loading.

Appendix C. Numerical Implementation of the Mixed Finite Element Formulation

The variational principle of this formulation proposed by Simo and Taylor (1991) incorporates the current displacement $\boldsymbol{u}$, dilation θ and the pressure p as the field variables. The finite element interpolation function of the displacement field is $\boldsymbol{N}$ and $\boldsymbol{\Gamma}$ is that of the other two fields. The resulting components of residual vector for each node in an element can be written as

$$\boldsymbol{R}_i^e = \boldsymbol{f}_{\text{ext},i}^e - \int_{\mathscr{B}} \boldsymbol{B}_i^T \boldsymbol{\tau} \, \mathrm{d}V \,. \tag{C.1}$$

In the above equation, $\boldsymbol{B}$ is the symmetric gradient of $\boldsymbol{N}$ in the current configuration, and the Kirchhoff stress tensor is calculated from (63) and the field variable p as

$$\boldsymbol{\tau} = pJ\boldsymbol{1} + \bar{\boldsymbol{\tau}} \qquad \text{where} \qquad J = \det\boldsymbol{F} \,. \tag{C.2}$$

The tangent for this formulation can be decomposed into 3 main parts namely material, geometric and pressure. The material part of the tangent can be written as

$$\boldsymbol{K}_{m,ij}^e = \int_{\mathscr{B}} \boldsymbol{B}_i^T \mathbb{C} \boldsymbol{B}_j \, \mathrm{d}V \,. \tag{C.3}$$

The expression for the spatial consistent tangent can expressed using (64), field variable p and (63) as

$$\mathbb{C} = pJ\left(\boldsymbol{1}\otimes\boldsymbol{1} - 2\mathbb{I}\right) + \mathbb{P}^T : \left[\bar{\mathbb{C}} + \frac{2}{3}\left(\bar{\boldsymbol{\tau}} : \boldsymbol{1}\right)\mathbb{I}\right] : \mathbb{P} - \frac{2}{3}\left(\mathbb{P}^T : \bar{\boldsymbol{\tau}}\otimes\boldsymbol{1} + \boldsymbol{1}\otimes\bar{\boldsymbol{\tau}} : \mathbb{P}\right) . \tag{C.4}$$

The geometric part of the tangent between nodes i and j can be written as

$$\boldsymbol{K}_{g,ij}^e = \left(\int_{\mathscr{B}} \nabla^T N_i \, \bar{\boldsymbol{\tau}} \, \nabla N_j \, \mathrm{d}V\right) \boldsymbol{1} \,. \tag{C.5}$$

The pressure tangent can be expressed as

$$\boldsymbol{K}^{e}_{p,ij} = \int_{\mathscr{B}} U''(\theta)\, \theta^{-1} \bar{\boldsymbol{b}}_i \bar{\boldsymbol{b}}_j^{\,T} \, \mathrm{d}V \,. \tag{C.6}$$

The expressions of the terms used in the above equation are

$$\bar{\boldsymbol{b}} = \left(\boldsymbol{\Gamma}^T \boldsymbol{H}^{-1} \int_{\mathscr{B}} \boldsymbol{\Gamma} \boldsymbol{b}^T J \, \mathrm{d}V \right)^T \tag{C.7}$$

$$\boldsymbol{H} = \int_{\mathscr{B}} \boldsymbol{\Gamma}\boldsymbol{\Gamma}^T \, \mathrm{d}V \tag{C.8}$$

$$\theta = \boldsymbol{\Gamma}^T \boldsymbol{H}^{-1} \int_{\mathscr{B}} \boldsymbol{\Gamma} J \, \mathrm{d}V \,. \tag{C.9}$$

In (C.7), $\boldsymbol{b}$ is the finite element interpolation for $\operatorname{div} \boldsymbol{u}$. The total tangent is obtained by adding all the three parts obtained in (C.3), (C.5) and (C.6).

Augmented Lagrangian method is utilized for imposing the incompressibility constraint to the problem. A suitable function of the field variable θ, $h(\theta)$, is forced to become zero by a Lagrange multiplier λ. The resulting pressure field variable p is calculated using

$$p = \kappa \gamma'(\theta) + \lambda h'(\theta) \,. \tag{C.10}$$

Uzawa's nested iteration algorithm is adopted for solving the system by updating the Lagrange multiplier λ after each augmented Lagrangian iteration n as

$$\lambda_{n+1} = \lambda_n + \kappa h'(\theta) \,. \tag{C.11}$$

The form of $U''(\theta)$ is adopted from the original work by Simo and Taylor (1991) as

$$U''(\theta) = \kappa \gamma''(\theta) + \lambda h''(\theta) \,. \tag{C.12}$$

However, the expressions for the functions $\gamma(\theta)$ and $h(\theta)$ as used by Weiss et al. (1996) produced better numerical convergence in our studies.

$$\gamma(\theta) = \tfrac{1}{2} \, (\ln \theta)^2 \;, \quad h(\theta) = \ln \theta \tag{C.13}$$

The parameter κ is analogous to the bulk modulus of the material. A suitable high value of $\kappa = 250$ was used initially and was increased with each augmented Lagrangian iteration for better convergence as done in Simo and Taylor (1991).

Appendix D. Comparison of fracture initiation using MAPC and eight-chain network model

A study was performed to compare the fracture initiation point of an elastomer modeled using the Maximal Advance Path Constraint method which is used in this study against the eight-chain network model developed by Arruda and Boyce (1993) for non-crystallizing rubbers. The formulation of the fracture initiation of an elastomer using the eight-chain model was followed from the study by Mao et al. (2017) with the expression of the internal energy due to bond stretch ε_b given by (8). The parameters used for the uniaxial tensile study of an unnotched specimen are tabulated in Table D.9.

Table D.9: Parameters used for the comparison study of the fracture initiation point using MAPC and eight-chain network model

μ	N	$E = nE_b$	$\varepsilon^f_{\mathrm{cr}} = nN\varepsilon^f_b$
0.37 MPa	18.5	925 MPa	515 MPa

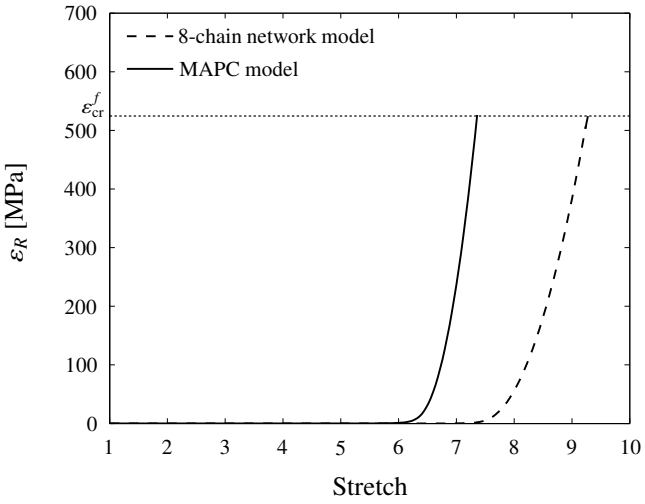

Figure D.23: Comparison of the fracture initiation points using MAPC and eight-chain network model

The expression of the internal energy due to bond stretch considered for rupture ε_R can be defined as

$$\varepsilon_{R,8-chain} = nN\varepsilon_b\left(\bar{\lambda_b}\right), \quad \varepsilon_{R,MAPC} = \max_{l=1,\ldots,n_{\rm int}} nN\varepsilon_b\left(\lambda_{b,l}\right). \tag{D.1}$$

In the above equation, $\bar{\lambda_b}$ represents the effective bond stretch which is the same in each chain along the eight principal stretch directions of a cubic volume and $\lambda_{b,l}$ stands for the bond stretch in a chain initially in the l-th quadrature direction. So, the internal energy due to bond stretch obtained in the case of the eight-chain model need not necessarily capture the maximum value among all directions unlike our model. With an increase in the number of quadrature directions considered for the numerical study, the current model captures the maximum value with greater precision.

The evolution of the quantity ε_R, which is used in the fracture initiation criterion given by (35), is plotted for both the models for the same set of parameters, as shown in Fig. D.23. It can be clearly seen that the fracture initiation criterion from our study is conservative as compared to the study by Mao et al. (2017). As the MAPC model accounts for anisotropy and considers the maximum value of the internal bond energy among chains in all the integration directions, it predicts an earlier fracture initiation as compared to the eight-chain model which considers an effective measure observing only the chains along the eight principal stretch directions of a cubic volume.

References

C. Li, H. Yang, Z. Suo, J. Tang, Fatigue-resistant elastomers, Journal of the Mechanics and Physics of Solids 134 (2020) 103751.

Y. Wang, C. Zhu, R. Pfattner, H. Yan, L. Jin, S. Chen, F. Molina-Lopez, F. Lissel, J. Liu, N. I. Rabiah, Z. Chen, J. W. Chung, C. Linder, M. F. Toney, B. Murmann, Z. Bao, A highly stretchable, transparent, and conductive polymer, Science Advances 3 (2017).

S. Wang, S. A. Chester, Experimental characterization and continuum modeling of inelasticity in filled rubber-like materials, International Journal of Solids and Structures 136 (2018) 125–136.

P. J. Loew, B. Peters, L. A. Beex, Rate-dependent phase-field damage modeling of rubber and its experimental parameter identification, Journal of the Mechanics and Physics of Solids 127 (2019) 266–294.

S. J. Hashemi, A. Sadooghi, K. Rahmani, S. Nokbehrosta, Experimental determining the mechanical and stiffness properties of natural rubber frt triangle elastic joint composite reinforcement by glass fibers and micro/nano particles, Polymer Testing 85 (2020) 106461.

V. Mittal, J. K. Kim, K. Pal, et al., Recent advances in elastomeric nanocomposites, volume 9, Springer, 2011.

R. Clamroth, T. Kempermann, Comparison of methods for the determination of tear strength, Polymer testing 6 (1986) 3–35.

G. Lake, A. Thomas, The strength of highly elastic materials, Proceedings of the Royal Society of London. Series A. Mathematical and Physical Sciences 300 (1967) 108–119.

W. Mars, A. Fatemi, Factors that affect the fatigue life of rubber: a literature survey, Rubber Chemistry and Technology 77 (2004) 391–412.

S. Toki, The effect of strain-induced crystallization (sic) on the physical properties of natural rubber (nr), in: Chemistry, Manufacture and Applications of Natural Rubber, Elsevier, 2014, pp. 135–167.

Y. L. Tee, M. S. Loo, A. Andriyana, Recent advances on fatigue of rubber after the literature survey by mars and fatemi in 2002 and 2004, International Journal of Fatigue 110 (2018) 115–129.

J. Katz, Röntgenspektrographische untersuchungen am gedehnten kautschuk und ihre mögliche bedeutung für das problem der dehnungseigenschaften dieser substanz, Naturwissenschaften 13 (1925) 410–416.
S. Gehman, J. Field, An x-ray investigation of crystallinity in rubber, Journal of Applied Physics 10 (1939) 564–572.
N. Candau, R. Laghmach, L. Chazeau, J.-M. Chenal, C. Gauthier, T. Biben, E. Munch, Strain-induced crystallization of natural rubber and cross-link densities heterogeneities, Macromolecules 47 (2014) 5815–5824.
S. Toki, I. Sics, S. Ran, L. Liu, B. S. Hsiao, Molecular orientation and structural development in vulcanized polyisoprene rubbers during uniaxial deformation by in situ synchrotron x-ray diffraction, Polymer 44 (2003) 6003–6011.
M. Tosaka, S. Murakami, S. Poompradub, S. Kohjiya, Y. Ikeda, S. Toki, I. Sics, B. S. Hsiao, Orientation and crystallization of natural rubber network as revealed by waxd using synchrotron radiation, Macromolecules 37 (2004) 3299–3309.
K. Brüning, K. Schneider, S. V. Roth, G. Heinrich, Kinetics of strain-induced crystallization in natural rubber studied by waxd: Dynamic and impact tensile experiments, Macromolecules 45 (2012) 7914–7919.
X. Chen, L. Meng, W. Zhang, K. Ye, C. Xie, D. Wang, W. Chen, M. Nan, S. Wang, L. Li, Frustrating strain-induced crystallization of natural rubber with biaxial stretch, ACS Applied Materials & Interfaces 11 (2019) 47535–47544.
P. Rublon, B. Huneau, E. Verron, N. Saintier, S. Beurrot, A. Leygue, C. Mocuta, D. Thiaudière, D. Berghezan, Multiaxial deformation and strain-induced crystallization around a fatigue crack in natural rubber, Engineering Fracture Mechanics 123 (2014) 59–69.
S. Trabelsi, P.-A. Albouy, J. Rault, Stress-induced crystallization around a crack tip in natural rubber, Macromolecules 35 (2002) 10054–10061.
H. Zhang, J. Niemczura, G. Dennis, K. Ravi-Chandar, M. Marder, Toughening effect of strain-induced crystallites in natural rubber, Physical review letters 102 (2009) 245503.
S. Gherib, L. Chazeau, J.-M. Pelletier, H. Satha, Influence of the filler type on the rupture behavior of filled elastomers, Journal of applied polymer science 118 (2010) 435–445.
K. Brüning, K. Schneider, G. Heinrich, In-situ structural characterization of rubber during deformation and fracture, in: Fracture mechanics and statistical mechanics of reinforced elastomeric blends, Springer, 2013a, pp. 43–80.
K. Brüning, K. Schneider, S. V. Roth, G. Heinrich, Strain-induced crystallization around a crack tip in natural rubber under dynamic load, Polymer 54 (2013b) 6200–6205.
P. J. Flory, Thermodynamics of crystallization in high polymers. i. crystallization induced by stretching, The Journal of Chemical Physics 15 (1947) 397–408.
K. Smith Jr, Crystallization of networks under stress, Polymer Engineering & Science 16 (1976) 168–175.
A. Gent, Crystallization and the relaxation of stress in stretched natural rubber vulcanizates, Transactions of the Faraday Society 50 (1954) 521–533.
M. Kroon, A constitutive model for strain-crystallising rubber-like materials, Mechanics of Materials 42 (2010) 873–885.
S. J. Mistry, S. Govindjee, A micro-mechanically based continuum model for strain-induced crystallization in natural rubber, International Journal of Solids and Structures 51 (2014) 530–539.
J. Guilie, T.-N. Le, P. Le Tallec, Micro-sphere model for strain-induced crystallisation and three-dimensional applications, Journal of the Mechanics and Physics of Solids 81 (2015) 58–74.
R. Rastak, C. Linder, A non-affine micro-macro approach to strain-crystallizing rubber-like materials, Journal of the Mechanics and Physics of Solids 111 (2018) 67–99.
V. N. Khiêm, M. Itskov, Analytical network-averaging of the tube model: Strain-induced crystallization in natural rubber, Journal of the Mechanics and Physics of Solids 116 (2018) 350–369.
A. Gros, E. Verron, B. Huneau, A physically-based model for strain-induced crystallization in natural rubber. part ii: Derivation of the mechanical model, Journal of the Mechanics and Physics of Solids 125 (2019) 255–275.
H. M. James, E. Guth, Theory of the elastic properties of rubber, The Journal of Chemical Physics 11 (1943) 455–481.
M. C. Wang, E. Guth, Statistical theory of networks of non-gaussian flexible chains, The Journal of Chemical Physics 20 (1952) 1144–1157.
E. M. Arruda, M. C. Boyce, A three-dimensional constitutive model for the large stretch behavior of rubber elastic materials, Journal of the Mechanics and Physics of Solids 41 (1993) 389–412.
C. Miehe, S. Göktepe, F. Lulei, A micro-macro approach to rubber-like materialspart i: the non-affine micro-sphere model of rubber elasticity, Journal of the Mechanics and Physics of Solids 52 (2004) 2617–2660.
M. Tkachuk, C. Linder, The maximal advance path constraint for the homogenization of materials with random network microstructure, Philosophical Magazine 92 (2012) 2779–2808.
A. A. Griffith, Vi. the phenomena of rupture and flow in solids, Philosophical transactions of the royal society of london. Series A, containing papers of a mathematical or physical character 221 (1921) 163–198.
R. Rivlin, A. G. Thomas, Rupture of rubber. i. characteristic energy for tearing, Journal of polymer science 10 (1953) 291–318.
N. A. Hocine, M. N. Abdelaziz, A. Imad, Fracture problems of rubbers: J-integral estimation based upon η factors and an investigation on the strain energy density distribution as a local criterion, International Journal of Fracture 117 (2002) 1–23.
S. Kawabata, Fracture and mechanical behavior of rubber-like polymers under finite deformation in biaxial stress field, Journal of Macromolecular Science, Part B 8 (1973) 605–630.
A. Hamdi, M. N. Abdelaziz, N. A. Hocine, P. Heuillet, N. Benseddiq, A fracture criterion of rubber-like materials under plane stress conditions, Polymer Testing 25 (2006) 994–1005.
A. Kumar, G. A. Francfort, O. Lopez-Pamies, Fracture and healing of elastomers: A phase-transition theory and numerical implementation, Journal of the Mechanics and Physics of Solids 112 (2018) 523–551.
A. Kumar, O. Lopez-Pamies, The phase-field approach to self-healable fracture of elastomers: A model accounting for fracture nucleation at large, with application to a class of conspicuous experiments, Theoretical and Applied Fracture Mechanics 107 (2020) 102550.
C. Chen, Z. Wang, Z. Suo, Flaw sensitivity of highly stretchable materials, Extreme Mechanics Letters 10 (2017) 50–57.
Y. Mao, B. Talamini, L. Anand, Rupture of polymers by chain scission, Extreme Mechanics Letters 13 (2017) 17–24.
B. Talamini, Y. Mao, L. Anand, Progressive damage and rupture in polymers, Journal of the Mechanics and Physics of Solids 111 (2018) 434–457.
G. Hamed, B. Park, The mechanism of carbon black reinforcement of sbr and nr vulcanizates, Rubber chemistry and technology 72 (1999)

946–959.
G. Hamed, Tearing of vulcanized rubber, Rubber chemistry and technology 78 (2005) 548–553.
W. Zhou, X. Li, J. Lu, N. Huang, L. Chen, Z. Qi, L. Li, H. Liang, Toughening mystery of natural rubber deciphered by double network incorporating hierarchical structures, Scientific reports 4 (2014) 1–6.
W. Kuhn, F. Grün, Beziehungen zwischen elastischen konstanten und dehnungsdoppelbrechung hochelastischer stoffe, Kolloid-Zeitschrift 101 (1942) 248–271.
S. Beurrot, B. Huneau, E. Verron, Strain-induced crystallization of natural rubber subjected to biaxial loading conditions as revealed by x-ray diffraction, Jerrams, S. et Murphy, N., éditeurs: Constitutive Models for Rubber 7 (2011) 23–28.
P. Flory, Thermodynamic relations for high elastic materials, Transactions of the Faraday Society 57 (1961) 829–838.
P. Wu, E. Van Der Giessen, On improved network models for rubber elasticity and their applications to orientation hardening in glassy polymers, Journal of the Mechanics and Physics of Solids 41 (1993) 427–456.
P. Bažant, B. Oh, Efficient numerical integration on the surface of a sphere, ZAMM-Journal of Applied Mathematics and Mechanics/Zeitschrift für Angewandte Mathematik und Mechanik 66 (1986) 37–49.
A. Thomas, Rupture of rubber. ii. the strain concentration at an incision, Journal of Polymer science 18 (1955) 177–188.
S. Trabelsi, P.-A. Albouy, J. Rault, Crystallization and melting processes in vulcanized stretched natural rubber, Macromolecules 36 (2003) 7624–7639.
J. Che, C. Burger, S. Toki, L. Rong, B. S. Hsiao, S. Amnuaypornsri, J. Sakdapipanich, Crystal and crystallites structure of natural rubber and synthetic cis-1, 4-polyisoprene by a new two dimensional wide angle x-ray diffraction simulation method. i. strain-induced crystallization, Macromolecules 46 (2013) 4520–4528.
J.-M. Chenal, L. Chazeau, L. Guy, Y. Bomal, C. Gauthier, Molecular weight between physical entanglements in natural rubber: A critical parameter during strain-induced crystallization, Polymer 48 (2007) 1042–1046.
G. R. Hamed, Molecular aspects of the fatigue and fracture of rubber, Rubber chemistry and technology 67 (1994) 529–536.
J. C. Simo, R. L. Taylor, Quasi-incompressible finite elasticity in principal stretches. continuum basis and numerical algorithms, Computer methods in applied mechanics and engineering 85 (1991) 273–310.
J. Marchal, Cristallisation des caoutchoucs chargés et non chargés sous contrainte: effet sur les chaînes amorphes, Ph.D. thesis, Universit Paris Sud - Paris XI, 2006.
J. Rault, J. Marchal, P. Judeinstein, P. Albouy, Chain orientation in natural rubber, part ii: 2 h-nmr study, The European Physical Journal E 21 (2006) 243–261.
A. Thomas, J. Whittle, Tensile rupture of rubber, Rubber Chemistry and Technology 43 (1970) 222–228.
G. Rong, G. Hamed, J. Jiang, Comparison of the strength of normal and edge-cut tensile specimens of styrene–butadiene rubber and natural rubber with similar crosslink density, Rubber Chemistry and Technology 89 (2016) 631–639.
J. A. Weiss, B. N. Maker, S. Govindjee, Finite element implementation of incompressible, transversely isotropic hyperelasticity, Computer methods in applied mechanics and engineering 135 (1996) 107–128.